University of Glasgow

DEPARTMENT OF

AEROSPACE ENGINEERING

The Development of a Prescribed Wake Model for the Prediction of the Aerodynamic Performance of Horizontal Axis Wind Turbines in Steady Axial Flow

by

D.J Robison, F.N Coton, R.A. McD Galbraith, M. Vezza

Departmental Report No. 9403

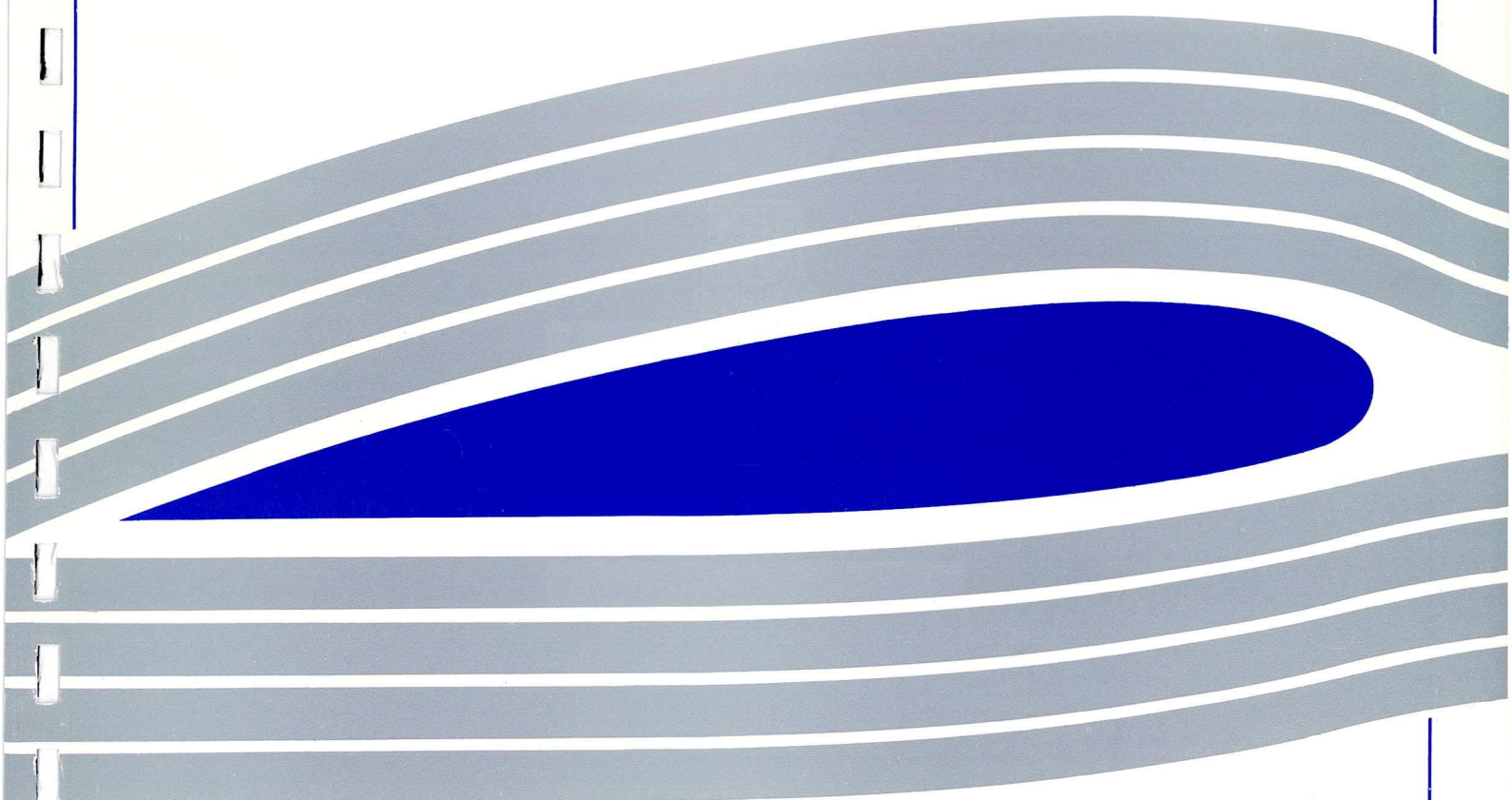

The Development of a Prescribed Wake Model for the Prediction of the Aerodynamic Performance of Horizontal Axis Wind Turbines in Steady Axial Flow

by

D.J Robison, F.N Coton, R.A. McD Galbraith, M. Vezza

Departmental Report No. 9403

March 1994

Department of Aerospace Engineering

University of Glasgow

Summary

The development of phase one of a new model for the prediction of the aerodynamic performance of horizontal axis wind turbines is described in the following report. At present the model is configured for performance prediction under steady axial flow conditions. Geometry prescription techniques, based on conservation of momentum, are employed to determine the shape of the turbine wake. This wake is modelled as a series of vortex filaments which, via the Biot-Savart relationship, allows the loadings on the turbine to be evaluated. As is the case with free wake models, a closed form solution is excluded due to the nature of the problem and iterative procedures are, therefore, used to obtain a good prediction. As well as a detailed description of the model, it's structure and the numerical procedures employed are described. The results obtained from the scheme are satisfactory at this stage of development but further validation is required. The work described in this report is intended to act as the basis for the development of a more comprehensive prescribed wake model, which should yield results of similar accuracy to free wake calculations while requiring only a fraction of the computational effort.

Nomenclature

a	Axial interference factor
a'	Rotational interference factor
c	Blade chord
C_D	Drag coefficient
C_L	Lift coefficient
C_N	Normal force coefficient
C_T	Tangential force coefficient
F	Far wake axial induced velocity parameter
L	Lift force
n	Number of blades
Q	Torque
r	Local radial position
R	Blade radius
t	Time
T	Thrust
T_{nw}	Time to far wake equilibrium
U_∞	Freestream velocity
v	Induced velocity
V_R	Local resultant velocity
α	Angle of attack
Γ	Vorticity
θ	Blade pitch
λ	Tip speed ratio
ρ	Air density
σ_L	Local blade solidity
ϕ	Blade inflow angle
ψ	Blade azimuth
ω_i	Induced angular velocity
Ω	Angular velocity

Subscripts :

1	Conditions near wake sub-region 1
2	Conditions near wake sub-region 2
3	Conditions near wake sub-region 3
b	Bound component
blade	Condition at blade
far	Condition in far wake
t	Trailed component
X	Radial component
Y	Tangential component
Z	Axial component

CONTENTS

1.	Introduction		1
2.	Model Description		4
	2.1	Overview of Model	4
	2.2	Coordinate System	5
	2.3	Blade model	5
	2.4	Model Start-up	7
	2.5	Wake Model	10
		2.5.1 General	10
		2.5.2 Wake Vorticity	11
		2.5.3 Vortex Wake Induced Velocity	12
		2.5.4 Vortex Wake Radius	14
		2.5.5 Trailing Vortex Roll-up	15
		2.5.6 The Near Wake	15
		2.5.7 Near Wake Geometry Prescription	16
		2.5.8 The Far Wake	17
		2.5.9 Determination of Wake Geometry Prescription Functions	18
3.	Numerical Procedure		22

3.1 System Characteristics Required as Input 22

3.2 Evaluation of Blade Initial Conditions 23

3.3 Evaluation of Blade Conditions For a Given Wake Geometry 23

3.4 Model Structure 26

4. Results and Discussion 28

5. Conclusions 31

6. Figures 32

Appendix A 65

Appendix B 66

References 69

1. Introduction

The flow around Horizontal Axis Wind Turbines (HAWT's) is complex and includes several sources of unsteadiness. Factors such as atmospheric turbulence, wind shear, the influence of the turbine tower on the blades and the active yawing of the turbine in response to large scale changes in wind direction, all contribute to the turbine operating environment. Additionally, in wind farms, the influence of the wakes from surrounding turbines may have a significant effect on blade inflow conditions. The cumulative effect of these phenomena results in the turbine blade experiencing unsteady loading, which has implications for both the aerodynamic performance of the turbine and the fatigue life of its structure.

In addition to the factors mentioned above, the practice of using blade stall as a method of regulating power output is another important influence on HAWT aerodynamic performance. Work carried out by Butterfield et al. [1] found that stall conditions on rotating wings differ significantly from those expected on wings in normal flight. No explanation of this phenomenon is available as yet, and so, prediction of this flow state is problematic. Moreover, if the turbine blades move in and out of stall at sufficiently high reduced frequencies, then the blades will be subject to dynamic stall. Investigations of this phenomenon have been carried out in the helicopter industry, but knowledge of its influence on the dynamic loading of wind turbine blades is limited.

The similarity between the aerodynamics of wind turbines, propellers and helicopter rotors has led to the adoption of similar methods of mathematical analysis. The simplest of these is momentum theory, which was first developed by Rankine in 1865. In this type of scheme, the rotor is represented as an actuator disk, across which exists a pressure drop. The flow through this disk is enclosed by a streamtube, which separates it from the freestream. The forces acting on the disk, the velocity at the disk and the power can then be evaluated by consideration of the mass flow rate, the change in kinetic energy and the momentum flux through the control volume. Momentum theory provides a good estimate of the average performance across the turbine blades. It's applications are, however, limited somewhat since it is unable to provide a more detailed indication of aerodynamic performance.

A modified version of momentum and blade element analysis, known as strip theory can be used to overcome some of the deficiencies of pure momentum models. This theory has evolved, but can be attributed to the original concepts of Lanchester and Flamm, with contributions from Joukowski and Betz. Examples of the application of

this analysis can be found in [2], [3] and [4]. As with momentum analysis, the rotor is replaced by an actuator disk with the flow through the disk enclosed by a streamtube. This streamtube is sub-divided into a number of concentric streamtubes. The induced velocities at the disk are then calculated by equating the forces obtained from momentum theory with those from blade element theory at each radial section of the disk. The velocity induced at the blade is considered to be uniform over the area of a given annular section.

Strip theory models are attractive due to their relative simplicity and the small amount of computing time required to obtain a solution. They have, thus, found much use in applications where the speed of calculation is of greater importance than accuracy. One drawback of strip theory, however, is that it does not directly take into account the induced effect of the turbine wake on the blades. The distribution of this induced flow is closely linked to the wake structure. The fact that strip theory models do not consider directly the wake structure imposes limits the application of this type of model, particularly in cases when the wake is concentrated near the turbine. In order to overcome this limitation, a mathematical model which includes a reasonable representation of the wake shape is desirable. One such group of models is free vortex or free wake models. This type of model employs vortex theory to obtain a detailed knowledge of the structure of the wake as a part of the model solution. As a result, a more realistic solution than is possible from the simple strip theory models may be obtained.

The strategy employed in free wake models is based on allowing the wake shape to deform under it's own influence until some steady state is achieved. From time zero, the induced effect of the wake on the blades is calculated at discrete azimuthal steps through application of the Biot-Savart law. The wake is gradually built up over a number of time steps as trailed and shed vorticity is added at each azimuthal position. The vorticity in the wake is modelled as a number of straight, finite vortex elements which are joined to form a piecewise continuous helical structure. An approximation of the wake shape is obtained at each time step by consideration of the induced effect on each wake element through successive application of the Biot-Savart law. Once a steady state representation of the wake structure is achieved a converged solution for the blade loadings can be obtained. Examples of the application of this type of model are detailed in [4], [5] and [6].

The value of free wake models lies in the detailed aerodynamic information which can be obtained from them. This type of model is, however, disadvantaged by the large

amount of computing time they require to achieve a solution. A less computationally intensive strategy would be to define the detailed wake geometry as part of the input to the problem rather than as part of the solution. Models which use this technique are termed prescribed wake models.

Central to the prescribed wake technique is the generation of mathematical functions which can give a good representation of the turbine wake geometry. Although the general nature of the flow behind a rotating system is known, this task is hindered by a lack of detailed knowledge of such flows. Through consideration of the induced velocity field at the blades and application of the principles governing fluid flow it is possible, however, to derive such functions. Once the the wake geometry is known, the wake vorticity and the rotor loads are calculated in the same manner as in free wake analyses. This technique has already been successfully applied to vertical axis wind turbine performance analysis, [7].

This report details the initial development stage of a prescribed wake model of a HAWT. The model, in its present form, is designed to estimate aerodynamic performance in steady, axial flow conditions. This represents the first stage in the development of a more comprehensive performance model which will calculate estimates of aerodynamic performance over a wide range of turbine configurations and operating conditions. A detailed description of the model follows in Chapter 2.

2. Model Description

2.1 Overview of Model

A prescribed wake model for the evaluation of the detailed aerodynamic performance of a horizontal axis wind turbine operating under axial flow conditions has been developed and is described below. The HAWTDAWG (Horizontal Axis Wind Turbine Directly Allocated Wake Geometry) model was developed using the following assumptions,

1. The flow is inviscid.

2. The fluid velocity is low enough for compressibility effects to be ignored.

3. The free stream flow is uniform and steady.

4. All blades are equally spaced, have identical geometry and aerodynamic characteristics.

The strategy employed in the HAWTDAWG model is the use of mathematical functions to prescribe the geometry of the vortex wake based on blade induced velocities. This means that the fully developed wake structure is established without regard to the wake self-induced velocities, as is the case with free wake models and, consequently, computation time is substantially reduced. The wake geometry is obtained in an iterative manner, from initial blade conditions estimated by application of a blade element/momentum analysis.

On the basis of this calculation an initial wake shape is generated using a number of polynomials which define the axial and radial development of the wake as functions of the induced velocities at the blades. Once this wake structure is known, the individual wake elements are assigned values of vorticity, corresponding to the variation in spanwise blade loading. New estimates of the velocities induced on the blades due to the influence of the wake are then calculated using vortex theory. These estimates differ from the original momentum calculations and so, as indicated above, an iterative procedure is employed to obtain a converged solution corresponding to the wake geometry.

Once this has been achieved, a revised wake geometry is constructed. The prescription functions employed to generate the initial wake are independent of the method used to estimate the blade induced velocities and so they are again used to prescribe the new wake geometry. The wake vorticity is then assigned and the influence of the wake on the blades calculated iteratively using vortex theory.

The process of revising the wake geometry to obtain new induced velocity estimates is repeated until a global convergence criterion has been satisfied. Once the final wake geometry has been derived a prediction of the aerodynamic performance of the rotor in the specified flow field can be obtained.

2.2 Coordinate Systems

The model uses both cartesian (X,Y,Z) and polar (r,ψ,Z) coordinates systems as defined in figure 2.1. An Earth fixed cartesian frame of reference defines the gross flow field, and the local blade conditions are defined by a rotating cartesian frame. The axis of rotation of the system corresponds to the positive Z axis of the cartesian frames. The X axis of the rotating frame lies along the blades. All induced velocities and general rotor performance characteristics are described using the Earth fixed axis set while local blade characteristics are described by the rotating axis set. The polar coordinate system has it's Z axis coincident with those of the cartesian frames and r is defined as the radial distance from the Z axis to any point in the spanwise direction. ψ describes the blade azimuthal position and is measured from the positive X axis of the Earth fixed cartesian system. Earth fixed parameters are transformed to rotating parameters using the following transformation

$$\begin{bmatrix} X' \\ Y' \\ Z' \end{bmatrix} = \begin{bmatrix} \cos\psi & \sin\psi & 0 \\ \sin\psi & -\cos\psi & 0 \\ 0 & 0 & 1 \end{bmatrix} \begin{bmatrix} X \\ Y \\ Z \end{bmatrix} \qquad (2.1)$$

2.3 Blade Model

Each blade is divided into a number of spanwise elements, which are aerodynamically independent. Conditions are assumed to be steady around the blade azimuth and so the aerodynamic performance of the blade elements may be obtained from steady two dimensional aerofoil data. The performance parameters, such as wake induced velocity and blade loading are calculated at control points, positioned at the quarter chord of the mid span of each cell. Values obtained at a given control point are then assumed to be

uniform over the whole blade element associated with that control point. A finer distribution of elements at the blade tip is employed to accommodate the large gradient in blade loading and the consequent strong trailing vorticity associated with the tip region.

The blade elements are defined by the positions of a series of element boundaries along the blade. The blade root section corresponds to the first blade element boundary, which is positioned at 0.1 of the blade radius. The remaining element boundary distribution along each blade is achieved using the following relationship

$$\frac{r}{R} = \frac{2}{\pi}\cos^{-1}\left[1 - \frac{(i-1)}{NE}\right] \qquad (2.2)$$

where R = blade radius
NE = number of blade elements
i = element boundary number ($i = 2 \rightarrow NE + 1$)
r = i_{th} element boundary position

A representative blade is shown in Fig 2.2

The bound vorticity, Γ_b, of each blade element is represented by a straight-line vortex which spans the element along the quarter chord line. The strength of the blade bound circulation is calculated using the Kutta-Joukowski theorem, which defines the relationship between the lift generated by an aerofoil and the circulation around it. For a blade element of width dr, chord c,with bound circulation Γ_b encountering a resultant velocity V_R, the lift generated is given by

$$L = \rho V_R \Gamma_b \, dr \qquad (2.3)$$

The lift on the blade element can also be expressed in the form,

$$L = \tfrac{1}{2}\rho c C_L V_R^2 \, dr \qquad (2.4)$$

From (2.3) and (2.4) we obtain the expression

$$\rho V_R \Gamma_b \, dr = \tfrac{1}{2}\rho c C_L V_R^2 \, dr \qquad (2.5)$$

Thus the bound circulation , Γ_b around the blade element is given by

$$\Gamma_b = \tfrac{1}{2} V_R c C_L \qquad (2.6)$$

The spanwise distribution of bound circulation can therefore be obtained by applying equation (2.6) to the control point of each blade element.

2.4 **Model Start-up**

The initial condition for free wake modelling is normally time zero, with the turbine at rest. When the turbine is started, the wake develops as time progresses. Hopefully a steady state is achieved in a reasonable time. The advantage of a prescribed wake model is that this stage is bypassed and iteration towards a converged result commences with a fully developed wake structure. Estimates of blade loading, necessary to provide data for the generation of an initial wake geometry, are obtained by applying momentum/blade element analysis (strip theory) to the turbine.

The rotor is modelled by an actuator disc which is divided into concentric, aerodynamically independent "streamtubes" or anulli. The induced spanwise velocity variation and blade loading can then be obtained by application of strip theory to each streamtube.

Applying the axial and angular momentum equations to a streamtube at radius r and width dr, Fig 2.3, the elemental thrust and torque components are given by

$$dT = d\dot{m}\, \Delta U \qquad (2.7)$$

and

$$dQ = d\dot{m}\, \Delta U_T r \qquad (2.8)$$

Expanding the above we obtain

$$\begin{aligned} dT &= 2\pi r \rho (U_\infty + v_z)\, dr \left(U_\infty - (U_\infty + 2v_z)\right) \\ &= -4\pi\rho\, r\, v_z (U_\infty + v_z)\, dr \end{aligned} \qquad (2.9)$$

and

$$\begin{aligned} dQ &= 2\pi\, r\rho (U_\infty + v_z)\, dr\, (2\omega_i r - 0)\, r \\ &= 4\pi \rho\, r^3 (U_\infty + v_z)\omega_i\, dr \end{aligned} \qquad (2.10)$$

where U_∞ = free stream velocity

v_Z = axial induced velocity at disk

$\omega_i = \frac{v_Y}{r}$ = rotational induced velocity at disk

Applying the velocities obtained from the momentum analysis to a blade element at radius r with width dr we obtain the velocity diagram shown in Fig 2.4. If it is assumed that the blade element acts like a two dimensional aerofoil, the non-dimensional normal and tangential components of the forces acting on the blade element are

$$\left.\begin{aligned} C_N &= C_L \cos\phi + C_D \sin\phi \\ C_T &= C_L \sin\phi - C_D \cos\phi \end{aligned}\right\} \qquad (2.11)$$

From these forces the elemental thrust and torque can be expressed as follows

$$dT = \frac{1}{2}\rho U_R^2 C_N n c \, dr \qquad (2.12)$$

$$dQ = \frac{1}{2}\rho U_R^2 C_T r n c \, dr \qquad (2.13)$$

where c = blade chord

n = number of blades

Equating the thrust obtained from momentum theory to that from blade element theory gives

$$-4\pi\rho r v_Z(U_\infty + v_Z)\, dr = \frac{1}{2}\rho U_R^2 C_N n c \, dr \qquad (2.14)$$

Which can be reduced to

$$-v_Z(U_\infty + v_Z) = \frac{U_R^2 C_N n c}{8\pi r} \qquad (2.15)$$

From Fig 2.4 the following relationships can be derived

$$U_R = \frac{U_\infty + v_Z}{\sin\phi} \qquad (2.16)$$

$$U_R = \frac{(\Omega + \omega_i)r}{\cos\phi} \tag{2.17}$$

which allows equation (2.15) to be written as

$$-v_Z(U_\infty + v_Z) = \frac{(U_\infty + v_Z)^2 C_N \sigma_L}{8 \sin^2\phi} \tag{2.18}$$

where σ_L is the local solidity

$$\sigma_L = \frac{n c}{\pi r} \tag{2.19}$$

Rearranging (2.18) gives

$$\frac{-v_Z}{U_\infty + v_Z} = \frac{\sigma_L C_N}{8 \sin^2\phi} \tag{2.20}$$

It is convenient to denote the axial induced velocity v_Z in non dimensional terms. This is normally done with respect to the free stream velocity, giving the term

$$a = \frac{-v_Z}{U_\infty} \tag{2.21}$$

which is known as the axial interference factor. Substituting (2.21) into (2.20) we obtain an expression in terms of the axial induced velocity at the rotor

$$\frac{a}{(1 - a)} = \frac{\sigma_L C_N}{8 \sin^2\phi} \tag{2.22}$$

Similarly, equating the expressions for torque obtained from momentum theory and blade element theory we obtain

$$4\pi\rho r^3(U_\infty + v_Z)\omega_i \, dr = \frac{1}{2}\rho U_R^2 C_T r n c \, dr \tag{2.23}$$

which reduces to

$$(U_\infty + v_Z)\omega_i = \frac{U_R^2 C_T n c}{8\pi r^2} \tag{2.24}$$

substituting equations (2.16) and (2.17) into (2.24) gives

$$(U_\infty + v_Z)\omega_i = \frac{(U_\infty + v_Z)(\Omega + \omega_i)\, r\, C_T\, \sigma_L}{8\, r \cos\phi \sin\phi} \qquad (2.25)$$

which yields

$$\frac{\omega_i}{(\Omega + \omega_i)} = \frac{C_T\, \sigma_L}{8\cos\phi \sin\phi} \qquad (2.26)$$

As with the axial induced velocity, it is convenient to denote the rotational induced velocity ω_i in non dimensional terms. This is normally done with respect to the blade rotational velocity, giving the term

$$a' = \frac{\omega_i}{\Omega} \qquad (2.27)$$

Which is the rotational interference factor. As with the axial case, substituting (2.27) into (2.26) gives the following expression for the induced rotational velocity at the rotor

$$\frac{a'}{(1 + a')} = \frac{\sigma_L\, C_T}{8\cos\phi \sin\phi} \qquad (2.28)$$

The spanwise variations of axial and rotational interference factors (and hence axial and rotational induced velocities), for a given rotor configuration operating in steady axial flow, are obtained using an iterative procedure which solves equations (2.22) and (2.28) at each blade element control point. This is discussed in more detail in Chapter 3. From these estimates of induced velocities an initial wake geometry can be constructed. The blade loadings can also be estimated, which means that the consequent wake vorticity distribution can be calculated. Thus, application of strip theory to the turbine yields sufficient information to obtain a reasonable representation of the fully developed wake which is the "starting point" for the model.

2.5 **Wake Model**

2.5.1 **General**

As air passes through the turbine, energy is removed from the flow. This results in a deceleration of the flow in the streamwise direction. Since momentum must be conserved, the radius of the wake will increase as the axial convection velocity

decreases. Thus, an axial contraction and a radial expansion of the wake occurs immediately behind the rotor. This continues until the wake achieves some far field equilibrium condition. The wake can therefore be viewed as consisting of two distinct regions. In the first of these, the near wake, large scale changes in the wake geometry occur before the equilibrium state is reached. Beyond this is the far wake region, which represents the new equilibrium state of the flow.

The wake of a HAWT consists of a continuous helical vortex sheet containing both trailed and shed vorticity. The trailed vorticity arises from the variation in spanwise bound vorticity while the shed vorticity is equal to azimuthal variations in blade bound vorticity. The current version of the HAWTDAWG model has been formulated for steady axial flow. For this limited case, blade conditions are steady around the azimuth and consequently, the wake will only contain trailed vorticity.

For this case the vortex wake is modelled as a discretised series of sequential finite straight-line vortex filaments which extend downstream from the blade trailing edge. These filaments are assumed to be solid bodies and trail downstream from the blades to the far field. The vorticity in the wake is assumed to be contained within the core of these filaments.

2.5.2 Wake Vorticity

The strength of the trailing vorticity in the wake is defined to be the difference between the bound vorticity on two adjacent blade elements. This is illustrated in Fig 2.5. If the strengths of blade elements i and i+1 are Γ_{bi} and Γ_{bi+1} respectively, then the strength of the vortex Γ_{tj}, trailed from the boundary between the two blade elements is defined as

$$\Gamma_{tj} = \Gamma_{bi+1} - \Gamma_{bi} \qquad (2.29)$$

For a blade with NE blade elements, eqn (2.29) defines the strengths of the NE+1 vortex elements trailed from the blade for a given spanwise bound vorticity distribution. Since the blade conditions are steady around the azimuth the strength of the vortex trailed between elements i and i+1, ($i = 1 \rightarrow NE$), will remain constant throughout the wake.

2.5.3 Vortex Wake Induced Velocity

A knowledge of the velocities induced at the blades due to the wake is required in order to calculate rotor performance. The induced velocity at a point due to a single wake element may be obtained by application of the Biot-Savart law. The total induced velocity at each blade element is, therefore, obtained by summation of the velocities induced at the blade element control point by each element of the wake.

From application of the Biot-Savart law, the velocity induced at a spacial point P(X,Y,Z) from an infinitesimal vortex element of strength Γ, (see Fig 2.6), is given by

$$d\underline{V} = \frac{\Gamma}{4\pi}\frac{d\underline{l}\times\underline{r}}{|r^3|} \tag{2.30}$$

From equation (2.30) the magnitude of the elemental induced velocity is,

$$d|\underline{V}| = \frac{\Gamma}{4\pi}\frac{d|\underline{l}|\,|\underline{r}|\sin\theta}{|\underline{r}|^3}$$

$$= \frac{\Gamma}{4\pi}\frac{d|\underline{l}|\,|\underline{r}|\sin\theta}{|\underline{r}|^2} \tag{2.31}$$

From Fig 2.6,

$$|\underline{r}| = \frac{|\underline{r_P}|}{\sin\theta} \tag{2.32}$$

and

$$d|\underline{l}| = |\underline{r_P}|\,\mathrm{cosec}^2\theta\,d\theta \tag{2.33}$$

Substituting equations (2.32) and (2.33) into equation (2.31) yields

$$d|\underline{V}| = \frac{\Gamma}{4\pi}\frac{|\underline{r_P}|\mathrm{cosec}^2\theta\sin\theta\,d\theta}{|\underline{r_P}|^2/\sin^2\theta}$$

$$= \frac{\Gamma}{4\pi}\frac{\sin\theta}{|\underline{r_P}|}\,d\theta \tag{2.34}$$

The magnitude of the velocity induced by a straight-line vortex element AB is therefore given by,

$$|\underline{V}| = \frac{\Gamma}{4\pi}\int_{\theta A}^{\theta_B}\frac{\sin\theta}{|\underline{r_P}|}\,d\theta$$

$$\Rightarrow |\underline{V}| = \frac{\Gamma}{4\pi|\underline{r_P}|}(\cos\theta_A - \cos\theta_B) \qquad (2.35)$$

The wake vorticity in this study is modelled as a chain of vortex elements of finite length. From Fig 2.6, for a vortex element AB of finite length,

$$\cos\theta_A = \frac{\underline{r_A}\cdot\underline{r_{AB}}}{|\underline{r_A}||\underline{r_{AB}}|}\ ,\ \cos\theta_B = \frac{\underline{r_B}\cdot\underline{r_{AB}}}{|\underline{r_B}||\underline{r_{AB}}|} \qquad (2.36)$$

and

$$|\underline{r_P}| = \frac{|\underline{r_A}\times\underline{r_B}|}{|\underline{r_{AB}}|} \qquad (2.37)$$

Thus, the magnitude of the velocity induced by a finite vortex line AB is

$$|\underline{V}| = \frac{\Gamma|\underline{r_{AB}}|}{4\pi|\underline{r_A}\times\underline{r_B}|}\left(\frac{\underline{r_A}\cdot\underline{r_{AB}}}{|\underline{r_A}||\underline{r_{AB}}|} - \frac{\underline{r_B}\cdot\underline{r_{AB}}}{|\underline{r_B}||\underline{r_{AB}}|}\right)$$

$$\Rightarrow |\underline{V}| = \frac{\Gamma}{4\pi|\underline{r_A}\times\underline{r_B}|}\left(\frac{\underline{r_A}\cdot\underline{r_{AB}}}{|\underline{r_A}|} - \frac{\underline{r_B}\cdot\underline{r_{AB}}}{|\underline{r_B}|}\right) \qquad (2.38)$$

In vector notation equation (2.38) becomes

$$\underline{V} = \frac{\Gamma\,\underline{r_A}\times\underline{r_B}}{4\pi|\underline{r_A}\times\underline{r_B}|^2}\left(\frac{\underline{r_A}\cdot\underline{r_{AB}}}{|\underline{r_A}|} - \frac{\underline{r_B}\cdot\underline{r_{AB}}}{|\underline{r_B}|}\right) \qquad (2.39)$$

Where

$$\frac{\underline{r}_A \times \underline{r}_B}{\left|\underline{r}_A \times \underline{r}_B\right|}$$

is the unit vector normal to the plane APB.

Using the relationships derived in Appendix A in conjunction with equation (2.39) the following expressions for the velocity components induced at a point P(X,Y,Z) by a finite vortex AB are obtained,

$$\underline{v}_X = \frac{\Gamma\left[(Y - Y_A)(Z - Z_B) - (Y - Y_B)(Z - Z_A)\right]}{4\pi\left|\underline{r}_A \times \underline{r}_B\right|^2}\left(\frac{\underline{r}_A \cdot \underline{r}_{AB}}{\left|\underline{r}_A\right|} - \frac{\underline{r}_B \cdot \underline{r}_{AB}}{\left|\underline{r}_B\right|}\right) \tag{2.40a}$$

$$\underline{v}_Y = -\frac{\Gamma\left[(X - X_A)(Z - Z_B) - (X - X_B)(Z - Z_A)\right]}{4\pi\left|\underline{r}_A \times \underline{r}_B\right|^2}\left(\frac{\underline{r}_A \cdot \underline{r}_{AB}}{\left|\underline{r}_A\right|} - \frac{\underline{r}_B \cdot \underline{r}_{AB}}{\left|\underline{r}_B\right|}\right) \tag{2.40b}$$

$$\underline{v}_Z = \frac{\Gamma\left[(X - X_A)(Y - Y_B) - (X - X_B)(Y - Y_A)\right]}{4\pi\left|\underline{r}_A \times \underline{r}_B\right|^2}\left(\frac{\underline{r}_A \cdot \underline{r}_{AB}}{\left|\underline{r}_A\right|} - \frac{\underline{r}_B \cdot \underline{r}_{AB}}{\left|\underline{r}_B\right|}\right) \tag{2.40c}$$

Therefore, if the position in space of each vortex element in the wake is known it is possible to calculate the corresponding induced axial, radial and tangential velocity components at the blade by applying equations (2.40a) - (2.40c).

2.5.4 **Vortex Core Radius**

Application of the Biot-Savart law to the wakes of rotating systems such as wind turbines can, under certain flow conditions, introduce numerical instabilities, i.e where a vortex element passes very close to or lies on the blade control point under consideration. In order to avoid such this problem, the idea of a finite vortex core may be utilised. The Biot-Savart law is ,therefore, applied to the flow field beyond the core radius while a modified relationship between induced velocity and perpendicular distance from the vortex element is employed inside the core. This technique results in a

more representative estimate of the induced velocity. Several vortex core models have been developed for use in the analysis of helicopter rotor aerodynamics. Two examples of these are shown in Fig 2.7. The simplest application of this concept involves considering the velocity induced at a control point to be zero if the control point lies within the vortex core. This representation vortex core is of sufficient accuracy at this stage in the development of the HAWTDAWG model.

In addition to the type of core model used, the vortex core size must also be considered. This choice is made difficult since little information is available on the subject . Work carried out by Langrebe [8], however, suggests that a constant core size of one percent of the rotor radius, R, is sufficient. This was adopted in the development of a prescribed wake model for vertical axis wind turbines by Basuno [7] and was found to be adequate. As such, this core size is adopted in this analysis.

2.5.5 Trailing Vortex Roll-up

The radial velocity of the trailing vortices will vary with spanwise position. This leads to the possibility that a given trailed vortex element Γ_j may be convected to a radial position beyond that of the adjacent element Γ_{j+1}. In real flows this would result in the two vortices rotating about the local centre of vorticity as shown in Fig 2.8. This phenomenon is common in the wakes of HAWT's, occuring predominantly at the tip region, and is known as vortex roll-up.

Vortex roll-up is modeled in the following manner. If the radial position of a vortex element trailed from the i_{th} blade element exceeds that of elements trailed from the adjacent $i+1_{th}$ blade element then the two are combined to form a single element of strength $\Gamma_j + \Gamma_{j+1}$. This 'new' wake element is assumed to occupy the same spacial position as the original wake element trailed from the $i+1_{th}$ blade element.

2.5.6 The Near Wake

Of the two wake regions the near wake has the greatest influence on the rotor induced velocities. As such care must be taken when prescribing the development of this region. A major consideration is the extent of the near wake. By drawing parallels with wakes behind bluff bodies (such as flat disks or plates normal to the free stream) it may be suggested that as a first step the near wake size may simply be dependent on the rotor diameter, as described in [9]. The structure of the wake behind a given turbine, however, will vary considerably with the operating tip speed ratio.

The wake behind a rotor operating at a low tip speed ratio will be relatively extensive with the trailed vortex system being convected much further downstream from the blades in a given time period than if the rotor were operating at a high tip speed ratio. It therefore seems likely that the extent of the near wake region will vary spacially, depending on the HAWT operating conditions. This presents difficulties in constraining the near wake to a spatial cut-off condition which is applicable over a wide range of tip speed ratios.

This suggests that simply linking the cut-off point of the near wake to the rotor diameter may not provide a satisfactory result. A more appropriate solution is to express the near wake cut-off as a function of time. This allows the near wake region to vary spatially depending on operating conditions, whilst offering a universal near wake cut-off criterion.

2.5.7 Near Wake Geometry Prescription

The work carried out by Basuno [7], achieved good results through using correlation with momentum theory as a means of obtaining suitable wake structures. This approach is also used as the basis of the wake prescription in this work. As stated previously, a prescribed wake model relies on the use of mathematical functions to define the axial and radial development of the wake.

In order to avoid the use of higher order polynomials, or even spline functions, in the description of the wake development, the axial development of near wake is divided into three sub-regions. It is,therefore, possible to define the non-linear variation of axial velocity from the blades to the far field through the use of relatively simple functions.

Inside each sub-region the axial velocity is described by a linear function of time. The geometry 'prescription' functions in each of the three regions are defined in such a way as to give continuous wake development. This is illustrated in Fig 2.9.

By adopting this strategy, the parameters of each of the sub-regions can be varied semi-independently over a range of operating conditions. In this way a universal solution for the development of the axial velocity in the near wake may be obtained. Having defined the axial velocity in the near wake as a function of time, the positions of the nodes of individual vortex elements are simply obtained by integration of these functions.

The radial development of the near wake is addressed in a different fashion from the axial development described above. Two differing strategies are employed.

The first strategy, implemented during the construction of the initial wake structure, involves the application of continuity to each streamtube to obtain the far wake radial positions of the vortex elements. The radial development of the wake from the blades to the far wake is then defined in a similar manner to the axial development described above. The near wake is again divided into three sub-regions (corresponding to those used for axial development). Inside each sub-region, the radial positions of the wake elements are determined by a linear function of time. As in the axial case, the radial prescription functions join to give a continuous expansion to the far field condition.

Following the construction of the initial wake geometry, a strategy based on the radial induced velocities calculated at the blades is implemented. This approach is preferable to that used to obtain the initial geometry as it is based on actual velocities and avoids the limitations of the application of continuity.

As the wake develops towards it's far field equilibrium the radial velocity of the wake will decrease to zero. The manner in which this occurs is modelled by a single quadratic function of time spanning the entire near wake region, as opposed to the 'phased' development employed in the axial direction. The radial positions of the near wake elements are therefore described by a cubic function of time.

2.5.8 **The Far Wake**

The far wake describes the region extending downstream from the last point in the near wake, corresponding to $t = T_{nw}$ seconds, to infinity. The flow field in the far wake represents the equilibrium state of the flow leaving the rotor blades. Flow conditions are therefore assumed to remain steady throughout the far wake, resulting in a cylindrical, axis-symmetric flow field.

The conditions in the far wake are achieved under the following constraints :

1. Radial velocity decreases from v_{Xblade} to zero at start of far wake

2. Axial induced velocity increases from v_{Zblade} to $F \cdot v_{Zblade}$ at the start of the far wake, where $F = \frac{v_{Zfar}}{v_{Zblade}}$

Applying simple momentum theory to the system dictates that the axial induced velocity in the far wake is equal to twice that at the blades. This is an average value which is representative of the whole rotor. When considered in more detail, however, it is not unreasonable to expect this value to vary along the span, especially in the tip region. Accordingly, a function was developed, defining the equilibrium state of the axial induced velocity using a far wake velocity parameter, F. This is allowed to vary with spanwise position, yielding a more detailed solution than that from momentum theory.

2.5.9 Determination of Wake Geometry Prescription Functions

The influence of the wake geometry on the blade loadings is extremely complicated and involves several inter-dependent parameters. The most efficient manner by which to obtain a satisfactory near wake geometry is, therefore, to solve simultaneously for as many of these parameters as possible. To this end, the scheme adopted involves obtaining the spacial development of the near wake, together with the location of the near wake cut-off point and the far field axial induced velocity conditions, in one global calculation.

Calculation of these parameters was achieved through the implementation of an iterative procedure. A mesh of control points, positioned along wake streamtube boundaries, was set up, as illustrated in Fig 2.10. The local velocity at each control point was then calculated using vortex theory and was compared to the corresponding prescribed value. The prescription function parameters were then modified in light of any difference which existed between the two. Using this technique, the prescription functions were gradually adjusted to give the optimum comparison between the prescribed and calculated velocity profiles. This was carried out over a range of tip speed ratios, yielding a universal set of wake geometry prescription functions. Defined as follows :

Near wake cut-off point : $T_{nw} = \frac{7\pi R}{4U_\infty}$ sec

Axial Velocity Far Wake Condition :

$$F = 1.1426 + 5.1906\frac{r}{R} - 8.9882\left(\frac{r}{R}\right)^2 + 4.0263\left(\frac{r}{R}\right)^3 \qquad (2.41)$$

Axial Development

Sub-Region 1 : $t = 0 \rightarrow \frac{\pi R}{4U_\infty}$ sec

where t = 0 describes conditions at the blades

End Condition : 60% of full axial deceleration achieved

Velocity Prescription Function

$$\underline{V}_{Z1} = U_\infty(1-a) + \frac{12\,a\,U_\infty^2}{5\pi R}(1-F)t \tag{2.42}$$

Displacement Prescription Function

$$S_1 = U_\infty(1-a)t + \frac{6a\,U_\infty^2}{5\pi R}(1-F)t^2 \tag{2.43}$$

Sub-Region 2 : $t = \frac{\pi R}{4U_\infty} \rightarrow \frac{\pi R}{U_\infty}$ sec

End Condition : 90% of full axial deceleration achieved

Velocity Prescription Function

$$\underline{V}_{Z2} = U_\infty\left(1-\frac{a}{2}(1+F)\right) + \frac{2a\,U_\infty^2}{5\pi R}(1-F)t \tag{2.44}$$

Displacement Prescription Function

$$S_2 = -\frac{a\pi R(1-F)}{16} + U_\infty\left(1-\frac{a}{2}(1+F)\right)t + \frac{a\,U_\infty^2}{5\pi R}(1-F)t^2 \tag{2.45}$$

Sub-Region 3 : $t = \frac{\pi R}{U_\infty} \rightarrow T_{nw}$ sec

End Condition : far field equilibrium achieved
(full axial deceleration)

Velocity Prescription Function

$$\underline{V}_{Z3} = U_\infty\left(1-\frac{a}{30}(7+23F)\right) + \frac{2aU_\infty^2}{15\pi R}(1-F)t \tag{2.46}$$

Displacement Prescription Function

$$S_3 = -\frac{47a\pi R(1-F)}{240} + U_\infty\left(1-\frac{a}{30}(7+23F)\right)t + \frac{aU_\infty^2}{15\pi R}(1-F)t^2 \tag{2.47}$$

Radial Development

Initial Strategy :

Sub-Region 1 : $t = 0 \rightarrow \frac{2\pi}{\Omega_{\lambda 8}}$ sec

End Condition : 60% of full radial expansion achieved

Displacement Prescription function

$$r_{w1} = r_{blade} + \frac{12(r_{far}-r_{blade})U_\infty}{5\pi R}t \tag{2.48}$$

Sub-Region 2 : $t = \frac{\pi R}{4U_\infty} \rightarrow \frac{\pi R}{U_\infty}$ sec

End Condition : 90% of full radial expansion achieved

Displacement Prescription function

$$r_{w2} = r_{blade} + \frac{r_{far}-r_{blade}}{2} + \frac{2(r_{far}-r_{blade})U_\infty}{5\pi R}t \tag{2.49}$$

Sub-Region 3 : $t = \frac{\pi R}{U_\infty} \rightarrow T_{nw}$ sec

End Condition : far field equilibrium achieved
(full radial expansion)

Displacement Prescription function

$$r_{w3} = r_{blade} + \frac{23(r_{far} - r_{blade})}{30} + \frac{2(r_{far} - r_{blade})U_{\infty}}{15\pi R}t \tag{2.50}$$

Main Strategy : $t = 0 \rightarrow T_{nw}$ sec

End Condition : far field equilibrium achieved
($v_{Xw} = 0.0$, blade fixed coordinates)

Velocity Prescription Function

$$v_{Xw} = v_{Xblade}\left[1 - \frac{t}{T_{nw}}\left(2 - \frac{t}{T_{nw}}\right)\right] \tag{2.51}$$

Displacement Prescription Function

$$r_{w} = r_{blade} + v_{Xblade}\,t\left[1 - \frac{t}{T_{nw}}\left(1 - \frac{t}{3T_{nw}}\right)\right] \tag{2.52}$$

3. Numerical Procedure

3.1 System Characteristics Required as Input

The HAWTDAWG model is is intended to be used as a design tool. Thus, the user is required to provide details of the rotor system and the operating conditions which are to be modelled.

The following information is required as input :

Freestream velocity	U_∞
Number of time steps per revolution	NTI
Number of wake cycles	NCYC
Number of blades	n
Tip speed ratio	λ
Number of blade elements	NE
Rotor Radius	R
Blade root chord	c_R
Blade taper ratio	Λ
Spanwise pitch variation	$\frac{d\theta}{dr}$

In general the user is free to assign these system parameters in any way he wishes, however the following constraints should be bourne in mind.

The model is designed to deal with large scale horizontal axis wind turbines, hence the number of blades specified should be limited to that found on this type of system.

In its present form, the model is not designed to deal with large scale reverse flow regions, this should be bourne in mind when results are required at high tip speed ratios, where various reverse flow states may be induced.

The number of time steps per revolution must be exactly divisible by the number of blades specified in order to break the cycle down into discrete steps.

3.2 Evaluation of Blade Initial Conditions

The initial conditions at a given blade control point are evaluated from equations (2.22) and (2.28), using an iterative procedure. This is illustrated in Fig 3.1.

The procedure is started by assuming initial values of a and a', taken to be zero in this study. The blade inflow angle at a given spanwise position $\frac{r}{R}$ is then calculated using,

$$\phi = \tan^{-1}\left[\frac{(1-a)}{(1+a')\lambda\frac{r}{R}}\right] \qquad (3.1)$$

which is obtained from Fig 2.4.

Since the blade pitch variation is known, the angle of attack α can be calculated. From Fig 2.4

$$\alpha = \phi - \theta \qquad (3.2)$$

Having obtained the angle of attack, the aerodynamic force coefficients C_L and C_D can be obtained from 2-D data. Thus the normal and tangential force coefficients C_N and C_T can be calculated using equation (2.11). Equations (2.22) and (2.28) can now be utilised to give updated estimates for a and a'. If the new values of a and a' fulfil the convergence conditions the procedure is stopped, otherwise it is repeated (from the calculation of ϕ) until convergence is achieved.

The above procedure is applied to each radial station in turn, giving the initial induced velocity state across the blades. From these converged solutions initial blade loadings, wake geometry and wake vorticity can be estimated.

3.3 Evaluation of Blade Conditions for a Given Wake Geometry

A converged solution for the aerodynamic condition at the blades for a given wake geometry is obtained using a first order Newton iterative scheme.

From Fig 3.2, when attempting to solve for a single differentiable function f for f(c) = 0, the error term g will tend to zero. The error, g, can be expressed as follows,

$$g^{k+1} = g^k + \Delta c\, g'^k \tag{3.3}$$

For a system of equations, equation (3.3) can be written as

$$g_i^{k+1} = g_i^k + \Delta c_i \nabla g_{i,j}^k \tag{3.4}$$

where,

$$\Delta c_i^k = \begin{bmatrix} \Delta c_1^k \\ \Delta c_2^k \\ . \\ . \\ \Delta c_i^k \end{bmatrix} \quad , \quad g_i^k = \begin{bmatrix} g_1^k \\ g_2^k \\ . \\ . \\ g_i^k \end{bmatrix}$$

and

$$\nabla g_{i,j}^k = \begin{bmatrix} \frac{\partial g_1}{\partial c_1} & \frac{\partial g_1}{\partial c_2} & . & . & \frac{\partial g_1}{\partial c_i} \\ \frac{\partial g_2}{\partial c_1} & \frac{\partial g_2}{\partial c_2} & & & . \\ . & & . & & . \\ . & & & . & . \\ \frac{\partial g_j}{\partial c_1} & . & . & . & \frac{\partial g_j}{\partial c_i} \end{bmatrix}$$

The solution of the function requires the error to become zero. Thus equation (3.4) can be written as

$$-g_i^k = \nabla g_{i,j}^k \Delta c_i^k \tag{3.5}$$

Now, if the $n \times n$ matrix $\nabla g_{i,j}^k$ is invertable, equation (3.5) can be rearranged to give

$$\Delta c_i^k = - \nabla g_{i,j}^{k\,-1} g_i^k \tag{3.6}$$

The system of equations which we wish to evaluate give the induced velocities due to the vorticity present in the wake of a HAWT at n×NE control points on the turbine blades. The axial induced velocity at the n_{th} control point may be written as

$$v_{Zn}^{k+1} = v_{Zn}^k + \Delta v_{Zn}^k \tag{3.7}$$

Substituting equation (3.6) into equation (3.7) gives

$$v_{Zn}^{k+1} = v_{Zn}^{k} - \left[\nabla g_{n,m}^{k\ -1}\right] g_{n}^{k} \tag{3.8}$$

The velocities induced at the blades are a function of the trailed vorticity in the rotor wake, as described in Section 2.4.3. The error term g_n^k in equation (3.8) can therefore be expressed as

$$g_{n}^{k} = v_{Zn}^{k} - f(\Gamma_{t}) \tag{3.9}$$

Since the strength of the vorticity trailed from a given blade element boundary is constant throughout the downstream extent of the wake, equation (3.9) can be written as

$$g_{n}^{k} = v_{Zn}^{k} - \sum_{\substack{p=1 \\ q=1}}^{\substack{NCYC \\ NE+1}} \Gamma_{tp,q} \cdot G_{p,q} \tag{3.10}$$

where $G_{p,q}$ describes the geometric position, with respect to the n_{th} blade control point, of the vortex element trailed from the p_{th} blade element boundary after q time steps. $\Gamma_{tp,q}$ is the strength of the vortex element.

The wake trailed vorticity arises from the spanwise variation in blade bound vorticity, as defined by equation (2.29) i.e

$$\Gamma_{tp,q} = \Gamma_{bp+1} - \Gamma_{bp} \tag{3.11}$$

where the blade bound vorticity is defined by equation (2.6).

Substituting equation (3.11) into equation (3.10) gives

$$g_{n}^{k} = v_{Zn}^{k} - \sum_{\substack{p=1 \\ q=1}}^{\substack{NCYC \\ NE+1}} \left(\Gamma_{bp} - \Gamma_{bp-1}\right) G_{p,q} \tag{3.12}$$

From equation (3.12) the term $\nabla g_{i,j}^{k}$ in equation (3.4) becomes

$$\nabla g^{k}_{i,j} = \begin{bmatrix} \frac{\partial g_1}{\partial v_{Z1}} & \frac{\partial g_1}{\partial v_{Z2}} & \cdots & \frac{\partial g_1}{\partial v_{Zi}} \\ \frac{\partial g_2}{\partial v_{Z1}} & \frac{\partial g_2}{\partial v_{Z2}} & & \cdot \\ \cdot & & \cdot & \cdot \\ \cdot & & \cdot & \cdot \\ \frac{\partial g_j}{\partial v_{Z1}} & \cdots & \cdots & \frac{\partial g_j}{\partial v_{Zi}} \end{bmatrix} \qquad (3.13)$$

where

$$\frac{\partial g_j}{\partial v_{Zi}} = \frac{\partial v_{Zj}}{\partial v_{Zi}} - \frac{\partial}{\partial v_{Zi}} \sum_{\substack{p=1 \\ q=1}}^{\substack{NCYC \\ NE+1}} \left(\Gamma_{bp} - \Gamma_{bp-1}\right) G_{p,q} \qquad (3.14)$$

The evaluation of the individual terms in equation (3.14) is described in Appendix B.

Hence, equation (3.14) can be evaluated by successive application of equation (B.13) and therefore v^{k+1}_{Zn} can be evaluated by substitution into equation (3.8).

A converged solution for the spanwise variation in axial velocity induced by a given wake is obtained by repeated solving of equation (3.8) at each blade control point until sufficient accuracy has been achieved.

3.4 **Model Structure**

The HAWTDAWG model is constructed in a modular fashion, such that the range of the model may be extended by simply inserting new modules at the relevant points.

The overall calculation may be broken down into a number of separate tasks. The order in which these tasks are dealt with is illustrated in Fig 3.3.

The model is initiated by the user entering a number of parameters which define the system to be modelled. These are listed in Section 3.1.

After this step the first task carried out by the code is the definition of the blade model. Here, the blade element distribution is calculated and the spanwise chord and local solidity variation evaluated.

Once the blade geometry is specified, the initial conditions at the blades are evaluated using the procedure detailed in Section 3.2. These initial conditions are evaluated at radial positions corresponding to the blade element boundaries, as knowledge of the velocities at these points is required for the generation of the wake.

The initial wake geometry may now be generated, using the functions described in Sections 2.4.6.4 and 2.4.6.5.

In order to assign vorticity to the wake elements generated above, the bound circulation on the blades must first be calculated. This is achieved by applying equation (2.6) to each blade element control point. Initially, induced velocities at the control points, are taken to be the average of those already calculated at the element boundaries. Having evaluated the blade bound vorticity, the wake trailed vorticity may be assigned using the relationship defined in Section 2.4.2.

Vortex theory is then used to determine the induced velocity variation at the blades due to the wake, as described in Section 2.4.3. Once this variation has been calculated, the iterative scheme detailed in Section 3.3 is employed to obtain a converged solution.

Following this, a new wake is generated, based on the converged blade conditions. Using vortex theory, a new estimate of the blade loading is obtained.The iterative scheme mentioned above is again implemented, yielding a converged solution for this wake geometry.

This point in the model structure represents the first step in the global iterative scheme. A revised wake is constructed, again based on the converged blade conditions from the previous stage, and vortex theory is used to obtain values of blade induced velocities. A comparison between these induced velocities and those obtained from the previous stage is made. The difference between the two solutions is then checked against the the criteria set down for full convergence of the system. The above procedure is repeated until the global convergence criterion are satisfied.

4. Results and Discussion

The HAWT test configuration used for the purpose of assessing the HAWTDAWG model consisted of a two bladed rotor, of diameter 14.0m. The blades were untwisted, having a constant pitch angle of 4°, with a taper ratio of 0.25. Each blade was divided into 16 blade elements while the blade azimuth was split into 16 discrete steps. The aerofoil data used was taken from 2-D static tests on the NACA 0015 profile, [10]. A constant freestream velocity of 9 ms^{-1} was used in all tests. Results from a range of tip speed ratios were obtained.

The wake prescription functions given in Section 2.5.9 were developed by comparison of prescribed and calculated axial induced velocity conditions throughout the wake. Figures 4.1 - 4.6 show the extent to which prescribed and calculated axial velocity distributions compare for tip speed ratios 7.0 - 12.0.

It can be seen from these figures that, in general, there is good agreement between the induced velocity distributions prescribed by the model and those calculated from the application of vortex theory to streamtube boundaries in the wake. The two compare particularly well in the first sub-region of the near wake.This is extremely important as the largest influence on blade conditions comes from this region. The largest decelerations also occur immediately behind the turbine, so accurate modelling of the wake development in this part of the flow field is vital to the overall accuracy of the model.

The only region where large deviations occur between the prescribed and calculated developments is at the blade tip. The difficulties experienced in prescribing the induced velocities in the tip region were not unexpected. The flow conditions change rapidly here, ranging from the relatively weak vortex sheet inboard through a region of high vorticity to the steady conditions in the freestream. It is, therefore, not surprising that a relatively simple wake scheme such as that employed in the HAWTDAWG model would encounter difficulties in this region of the flow field.

Figure 4.7 shows a comparison between prescribed and calculated far wake axial induced velocity conditions. Again, with the exception of the tip region, the agreement is very good. With 64% of the calculated values of the far wake axial induced velocity parameter, F, falling within 0.05 of the prescribed values and all calculated values falling within 0.1 of those prescribed by equation (2.58).

The iterative development of the wake geometry produced by the model at tip speed ratio 9.0 is shown in Figure 4.8. For clarity, the figure shows the first five cycles of the vortex structure trailed from one of the HAWT blades in isolation.It can be observed that the largest change in the wake structure occurs between the first and second iterations. These correspond to the geometry prescribed from blade conditions calculated using strip theory and the first wake developed from vortex theory calculations. It is, therefore, not surprising that the greatest adjustment to the wake geometry is made at the change over between the two calculation strategies.

The similarity in the geometries produced by successive iterations of the vortex theory is encouraging with respect to the stability of the model. The fact that large fluctuations in the wake geometry do not occur from iteration to iteration would suggest that the overall model strategy is convergent in nature. Additionally, the overall structure of the wake seems reasonable and in general terms shows good agreement with the wake structure obtained by Bareiß and Wagner[11] using a free wake model.

The blade loading distributions over the range of test operating conditions are shown in Figures 4.9 - 4.14. Each figure presents the evolution of the blade loading patterns over eight iterations of the wake geometry. It can be seen that the overall convergence characteristics of the blade loadings are extremely good, with full convergence occurring by the eighth iteration at all tip speed ratios. It should be noted, however, that the high tip speed ratio cases require a greater number of iterations than the low and mid-range cases to reach a fully converged state. This is due to the highly compact nature of the wake under these inflow conditions. The result of this is a greater degree of fluctuation of blade conditions in the initial stages of the iterative process, which leads to a greater number of iterations being required to obtain a converged solution.

The figures show a shift in the spanwise position of the maximum loading, Γ_{max}, as the tip speed ratio increases. For $\lambda = 7.0$ (Fig 4.9), Γ_{max} occurs around the centre of the blade, but as λ increases it shifts gradually inboard towards the root. This inboard shift in the position of Γ_{max} is accompanied by a general increase in the magnitude of the loading on the inboard section of the blades. The magnitude of Γ_{max} itself,however, only increases slightly with tip speed ratio. The magnitude of the loading of the outboard section of the blades also remains relatively constant.

The manner in which the spanwise blade loading pattern varies with tip speed ratio may be due to the change in the blade inflow angle as λ increases. At low tip speed ratios a large section of the root region of the blades will be operating at high angles of attack,

i.e well into the stall region of the aerofoil section's aerodynamic performance envelope. As tip speed ratio increases the inflow angle will generally decrease across the span, mainly due to the increase in the tangential velocity component of the flow. Since the blade pitch variation is kept constant over the range of operating conditions, this decrease in inflow angle corresponds to a decrease in the effective angle of attack of the blades. If the angle of attack reduces sufficiently, inboard regions of the blades will move out stall, and realise an increase in the local C_L. In this way, the blade loading in this region will increase with tip speed ratio. Conversely, a decrease in the angle of attack in the outboard region of the blades means that, in performance terms, the aerofoil is moving down the linear section of the lift curve. Leading to a decrease in the local C_L in this region of the rotor. This is show in Figure 4.15. The fact that the magnitude of the loading on the tip region does not change significantly suggests that the decrease in C_L is counteracted by the increase in the relative velocity as tip speed ratio increases.

The spanwise axial induced velocity variation with tip speed ratio is shown in figures 4.16 - 4.21. The induced velocities in these figures were calculated at the mid-point of each blade element. Again the results correspond to operating tip speed ratios ranging from 7.0 - 12.0. As with the blade loading, the convergence characteristics are generally very good and the high tip speed ratio cases require a greater number of iterations to achieve full convergence.

A general spanwise increase in the magnitude of the induced velocity can be observed with increasing tip speed ratio. This increase is greatest on inboard regions of the blades and corresponds to the associated change in blade loadings. The overall shape of the spanwise distribution of induced velocity remains the same as λ increases, i.e it increases from the root value to some 'inboard peak' before decreasing until the tip region is reached where the magnitude again increases until an 'outboard peak' is reached at a position corresponding to the mid-point of the tip blade element. Although this general pattern exists over the range of tip speed ratios, the position of the maximum induced velocity changes as λ increases. At the low tip speed ratios, the maximum value occurs near the tip. As λ increases,however, the magnitudes of the induced velocities inboard increase rapidly until they are greater than those outboard. Thus, the maximum induced velocity is seen to shift from the 'outboard peak' at the tip region to an 'inboard peak'. The spanwise position of this 'inboard peak' also changes with tip speed ratio, shifting towards the root as λ increases, mirroring the change in spanwise position of Γ_{max} .

5. Conclusions

A prescribed wake model for the prediction of the performance of large scale horizontal axis wind turbines in axial flow has been developed. The wake structure produced appears qualatively similar to that of a free wake model and the blade loading and induced velocity patterns predicted are reasonable for the blade geometry and operating conditions specified. The model exhibits good overall convergence characteristics over the range of conditions considered in the study. This is encouraging from the point of view of the further development of the model which will undoubtedly be made more straightforward by virtue of the fact that the basic model is stable in nature.

Although the results produced by the model to date appear to be satisfactory, their accuracy cannot fully be assessed until validation against other numerical predictions and experimental data is carried out. Following this, it is hoped to develop the model further to give performance estimates in yawed flow conditions.

5. Conclusions

A prescribed wake model for the prediction of the performance of large scale horizontal axis wind turbines in axial flow has been developed. The wake structure produced appears qualatively similar to that of a free wake model and the blade loading and induced velocity patterns predicted are reasonable for the blade geometry and operating conditions specified. The model exhibits good overall convergence characteristics over the range of conditions considered in the study. This is encouraging from the point of view of the further development of the model which will undoubtedly be made more straightforward by virtue of the fact that the basic model is stable in nature.

Although the results produced by the model to date appear to be satisfactory, their accuracy cannot fully be assessed until validation against other numerical predictions and experimental data is carried out. Following this, it is hoped to develop the model further to give performance estimates in yawed flow conditions.

6. **Figures**

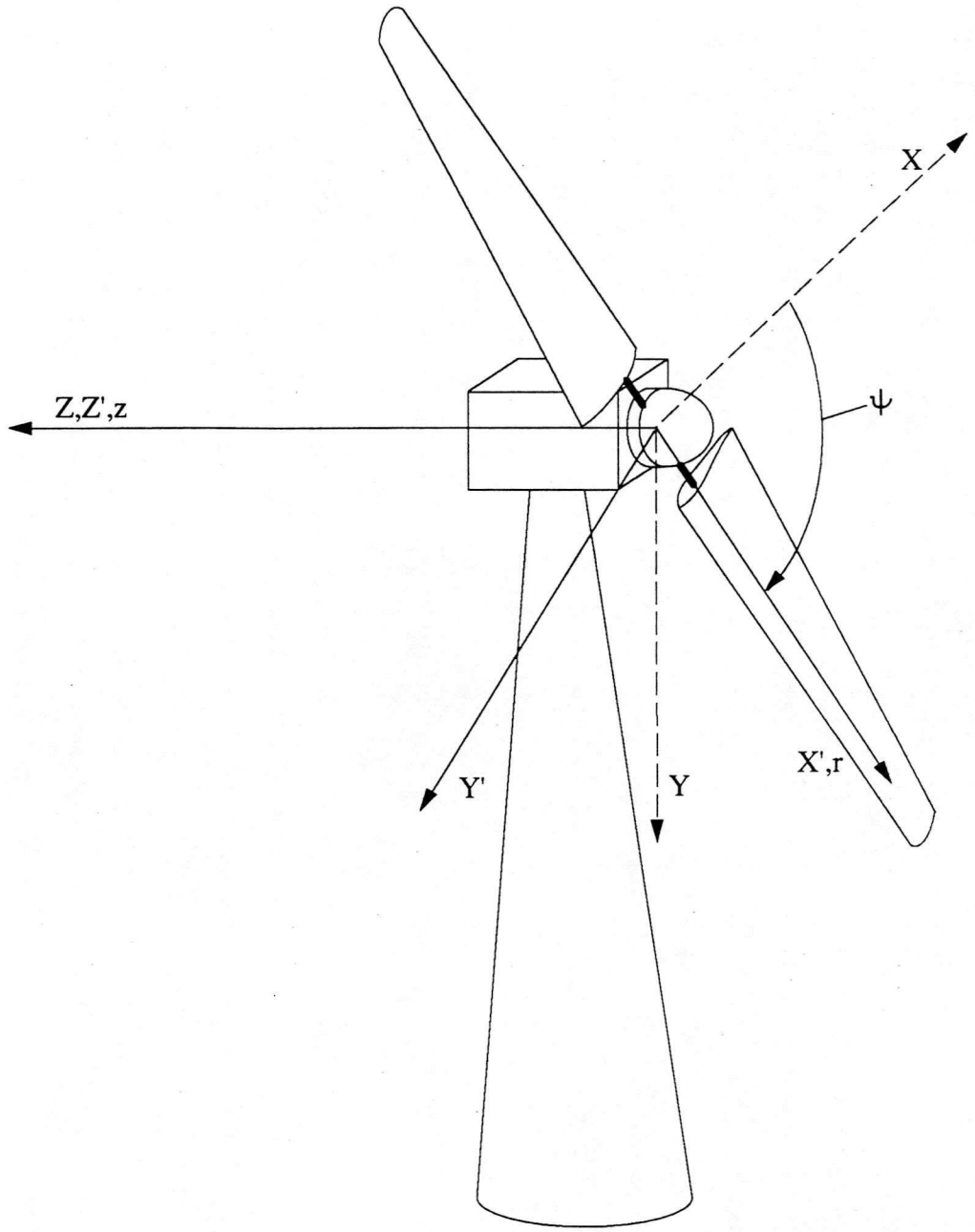

Figure 2.1 Model Coordinate System

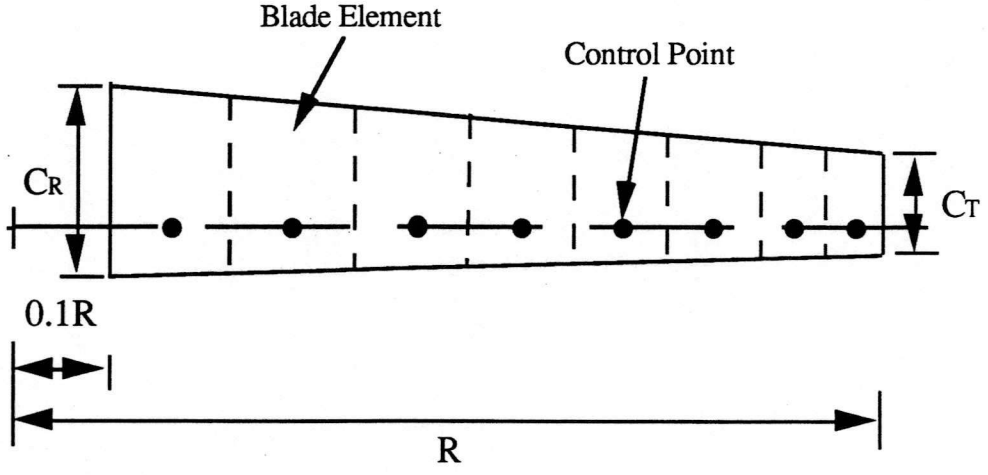

Figure 2.2 Representative Blade Element Distribution

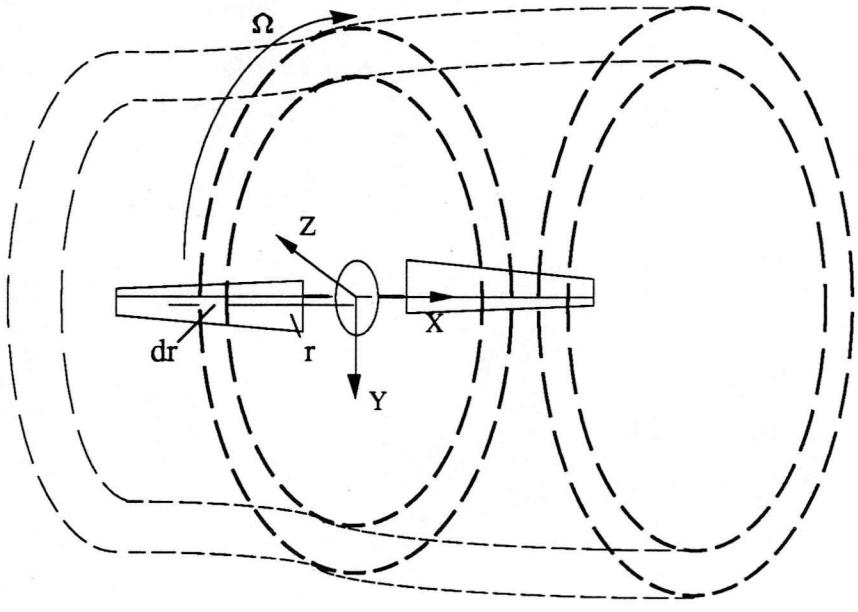

Figure 2.3 Streamtube Through Radial Position r

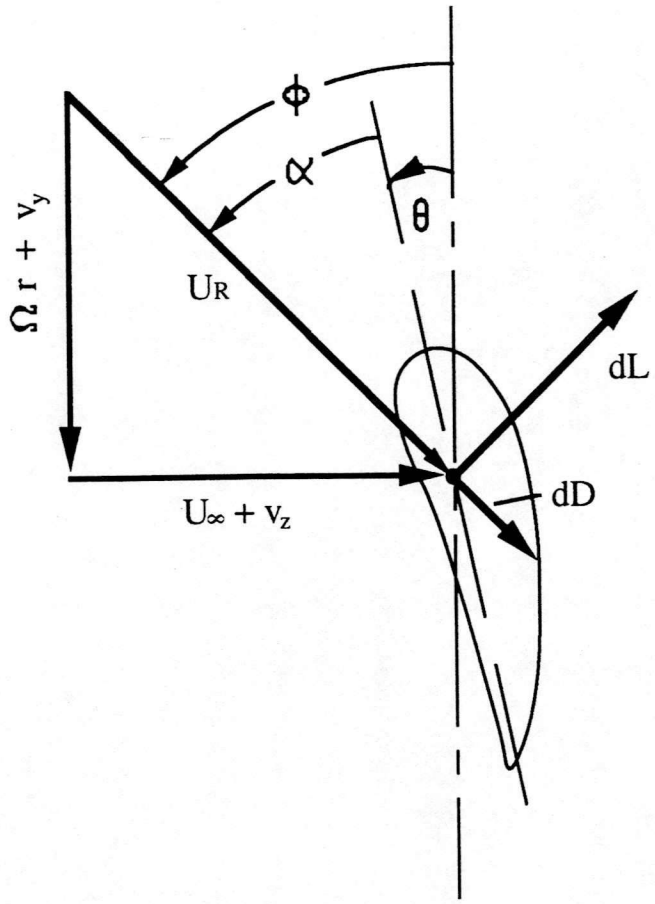

Figure 2.4 Velocity Diagram

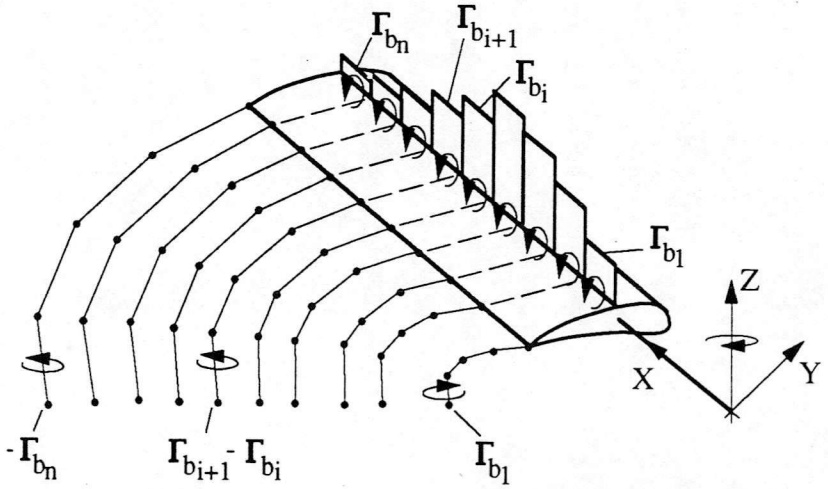

Figure 2.5 Trailed Vorticity Model

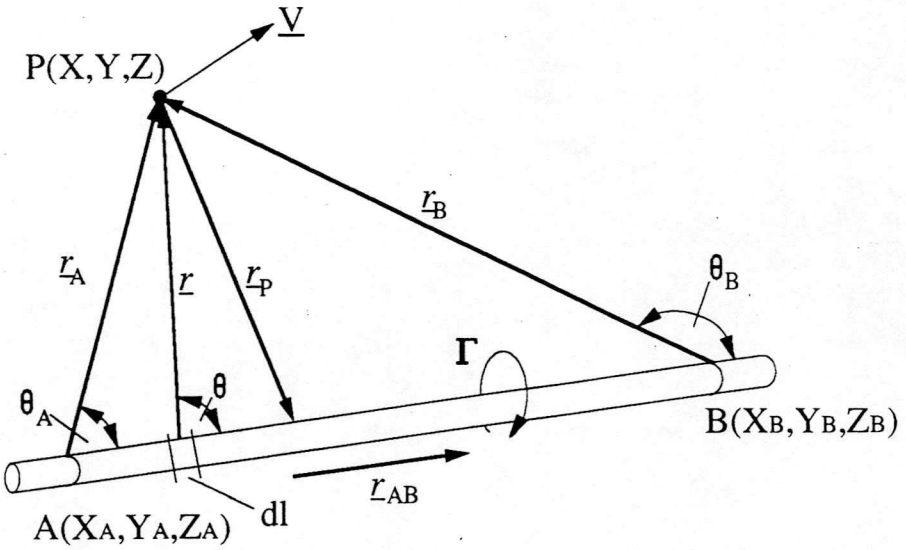

Figure 2.6 Velocity Induced by Vortex Element AB

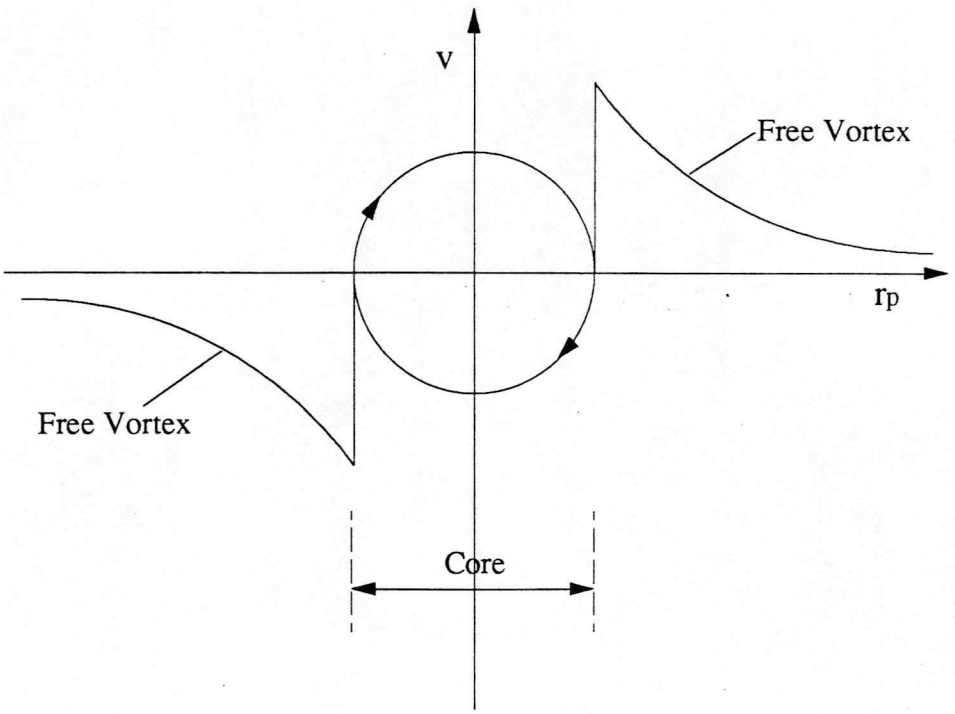

a)

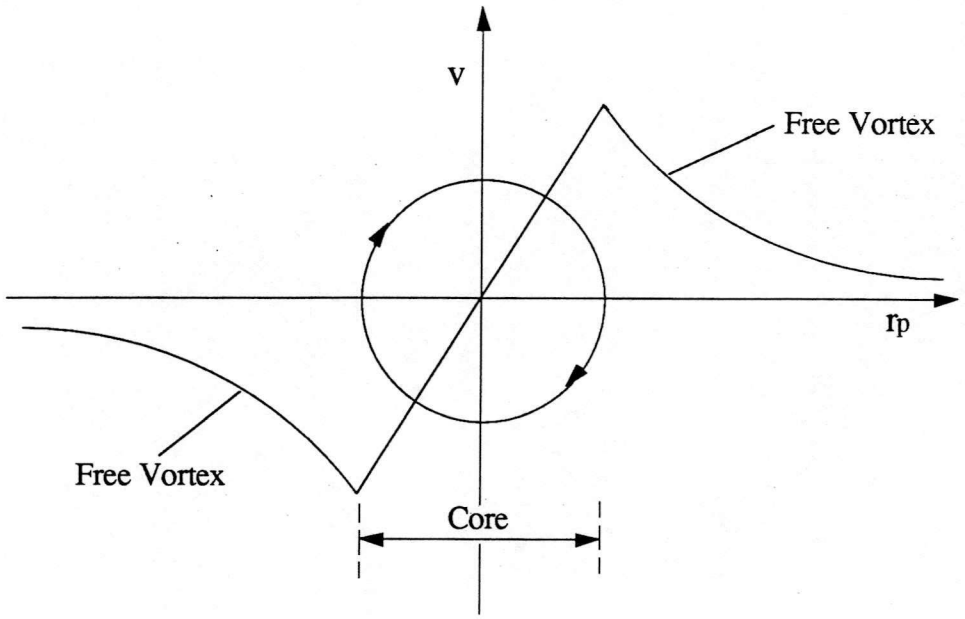

b)

Figure 2.7 Vortex Core Models

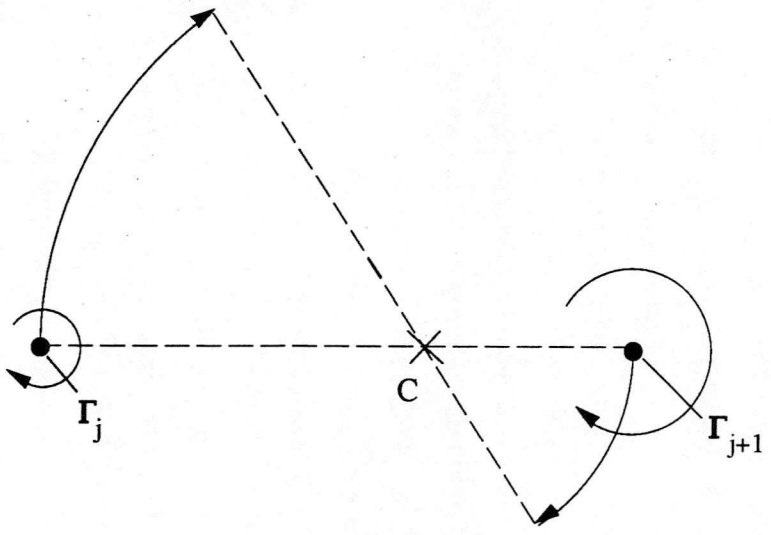

Figure 2.8 Relative Motion of Two Vortex Elements Around Local Centre of Vorticity

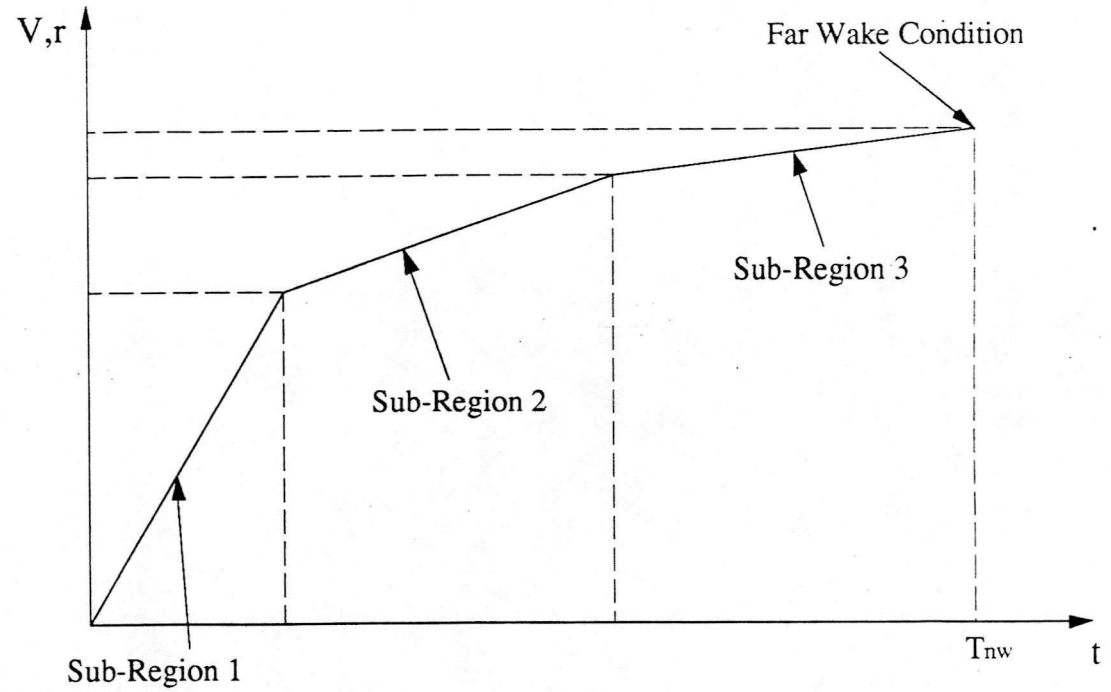

Figure 2.9 Development of Near Wake

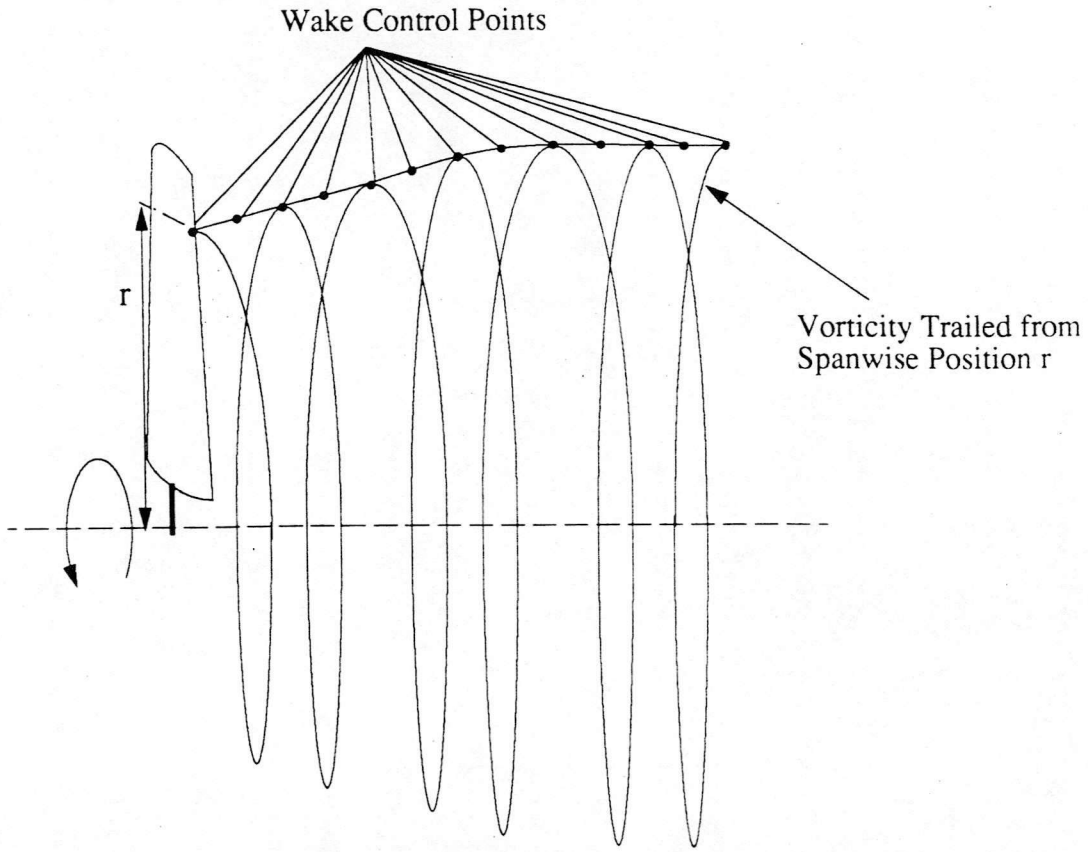

Figure 2.10 Positioning of Wake Control Points

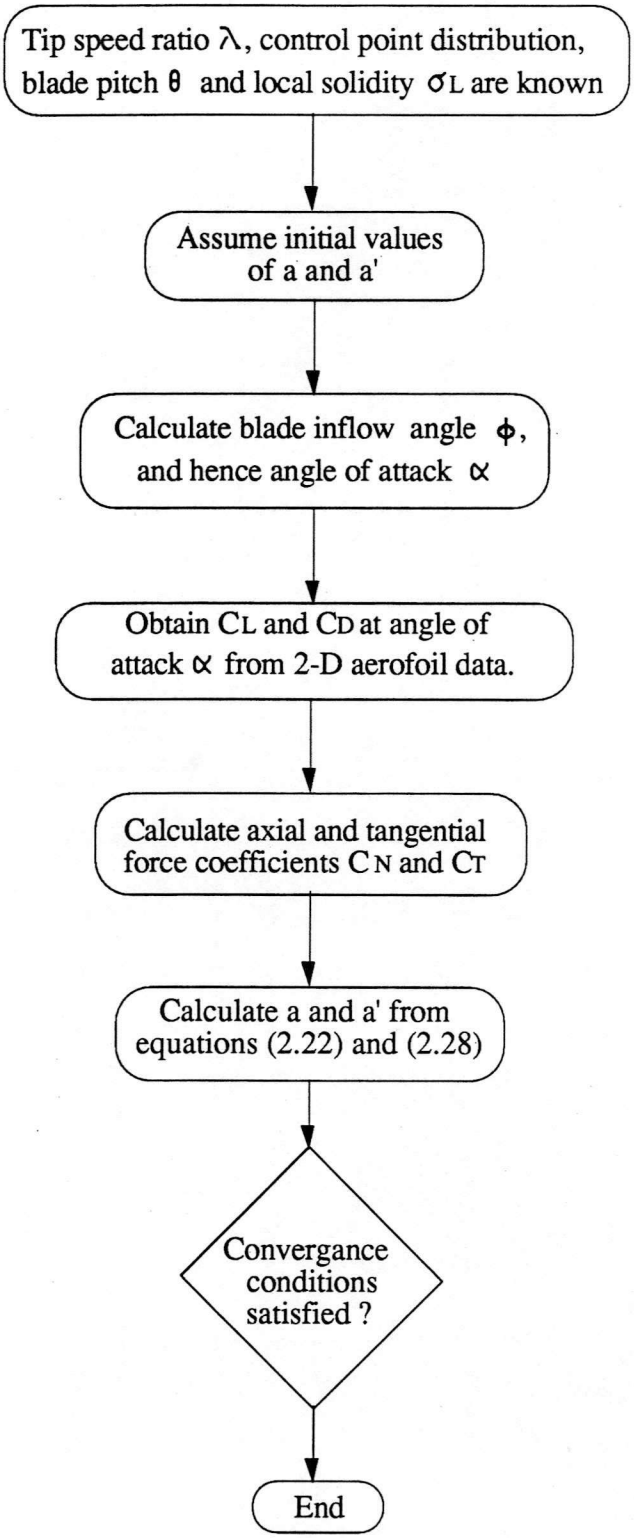

Figure 3.1 Strip Theory Iterative Procedure

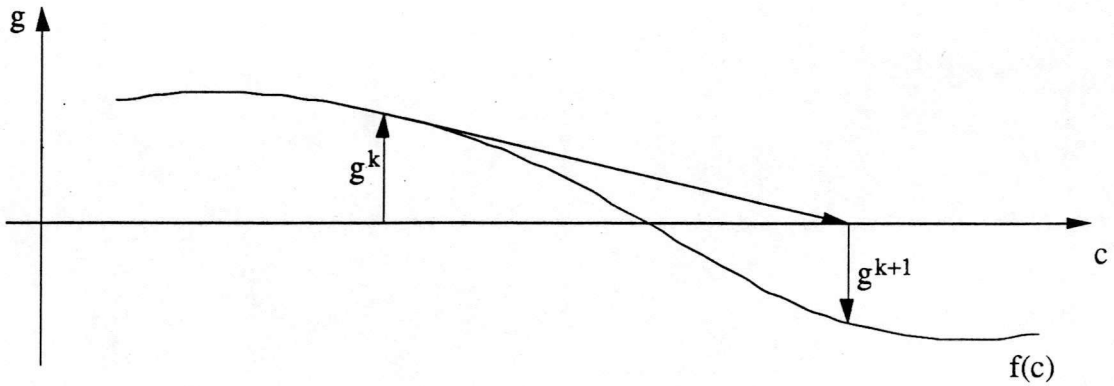

Figure 3.2 Iteration towards f(c)=0

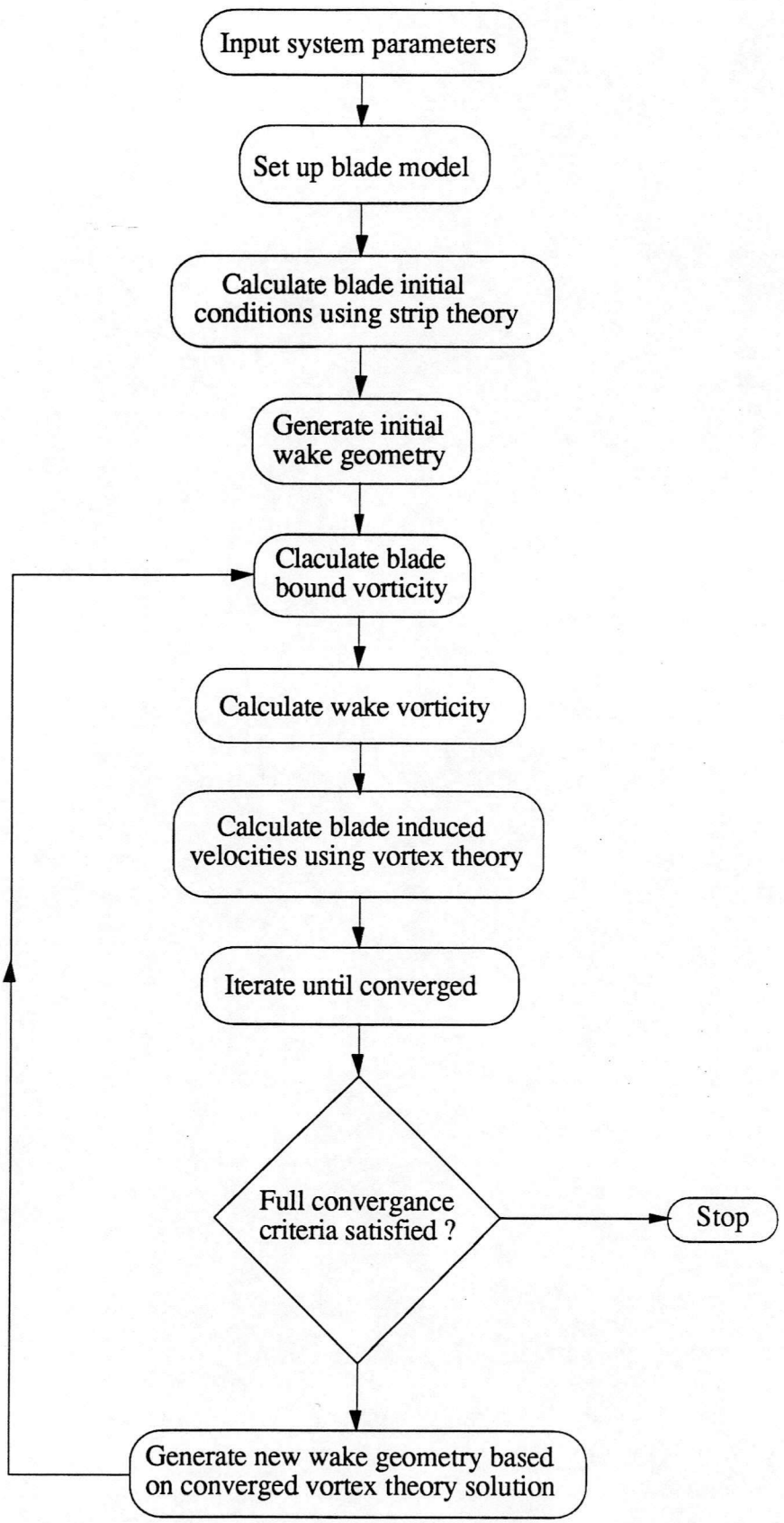

Figure 3.3 Model Structure

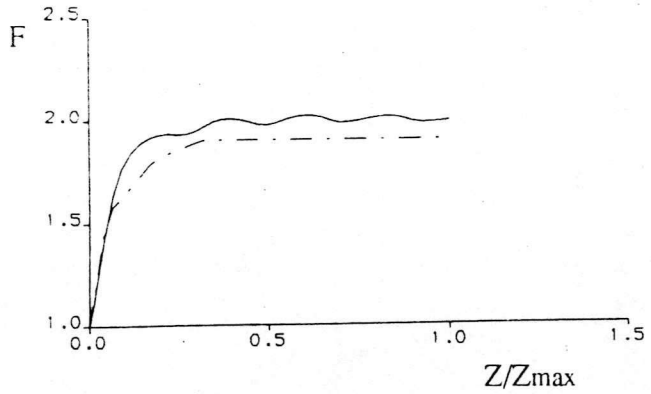

a) r/R = 0.226

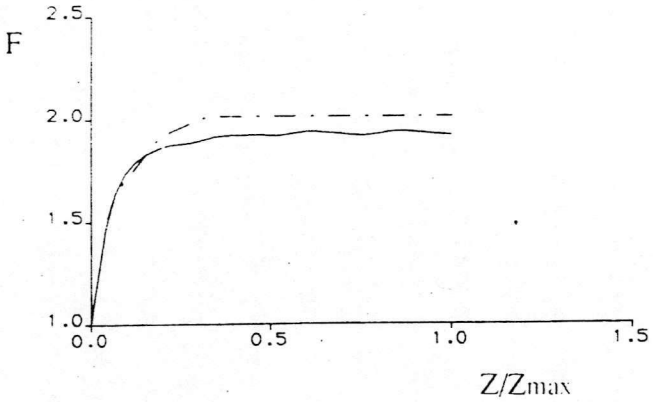

b) r/R = 0.321

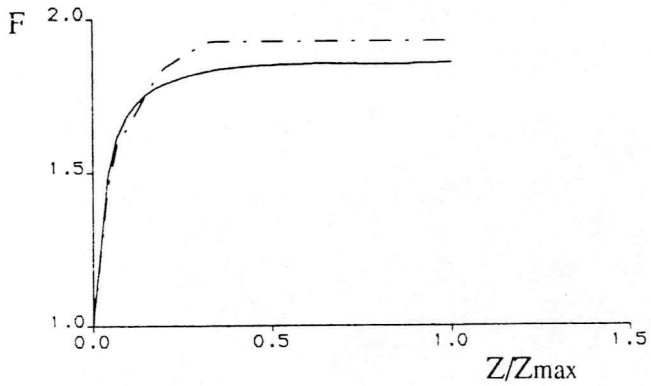

c) r/R = 0.570

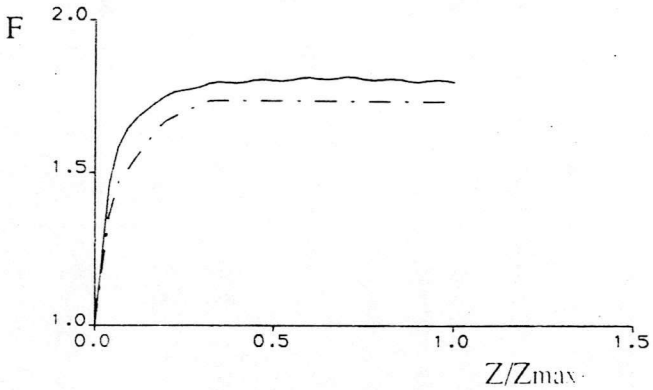

d) r/R = 0.771

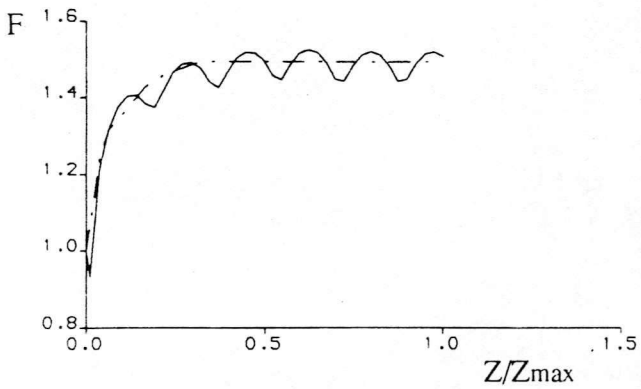

e) r/R = 0.880

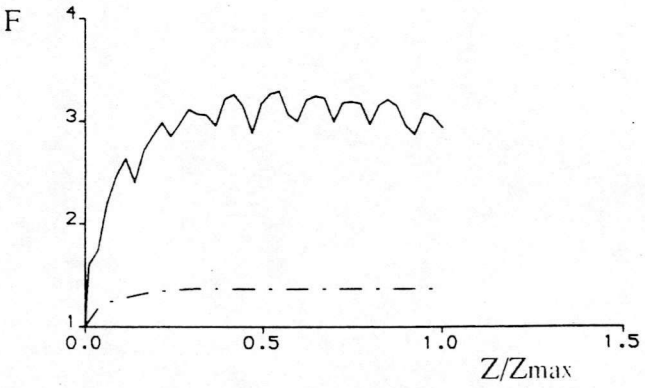

f) r/R = 1.0

Calculated ————————

Prescribed · — —— — ·

Figure 4.1 Comparison between prescribed and calculated axial induced velocities : $\lambda = 7.0$

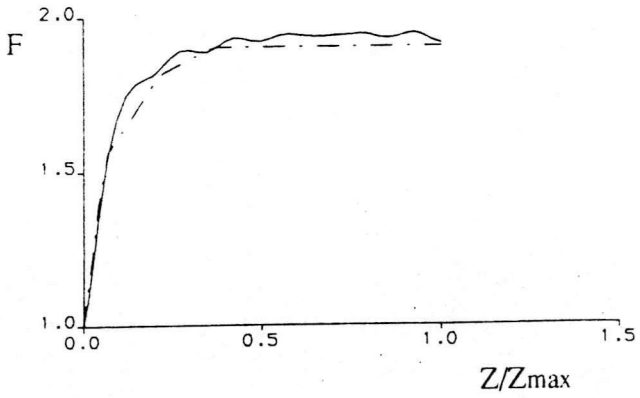

a) r/R = 0.226

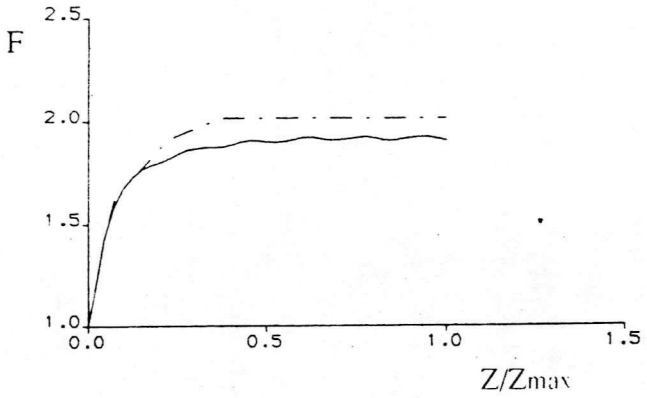

b) r/R = 0.321

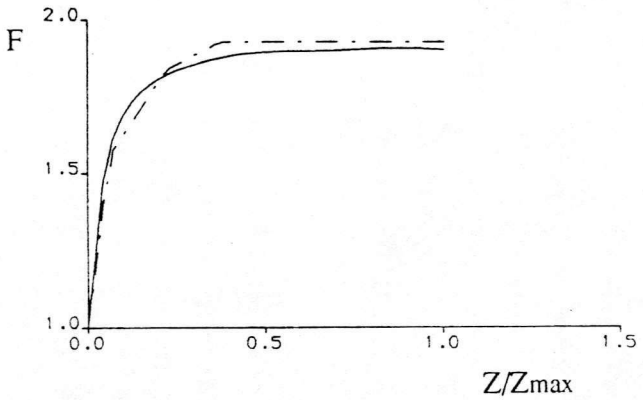

c) r/R = 0.570

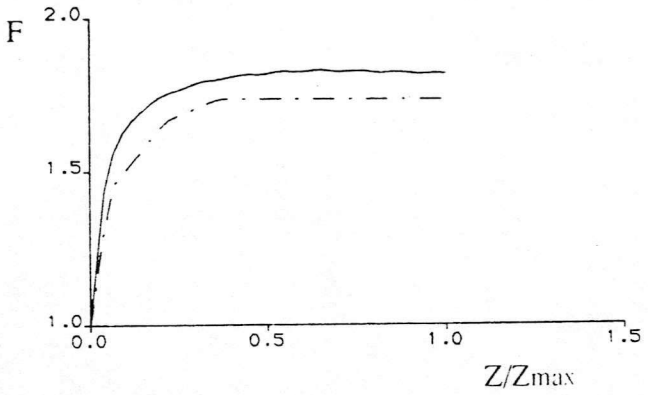

d) r/R = 0.771

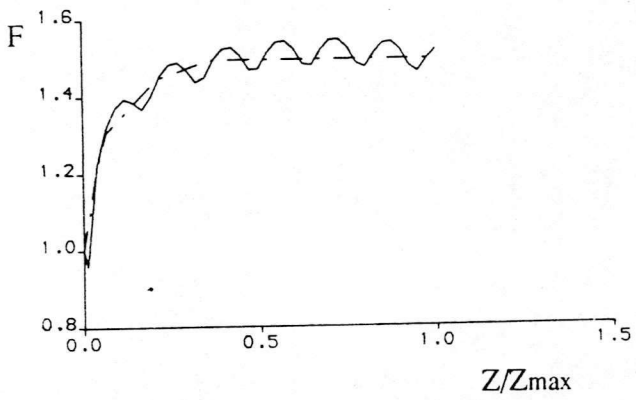

e) r/R = 0.880

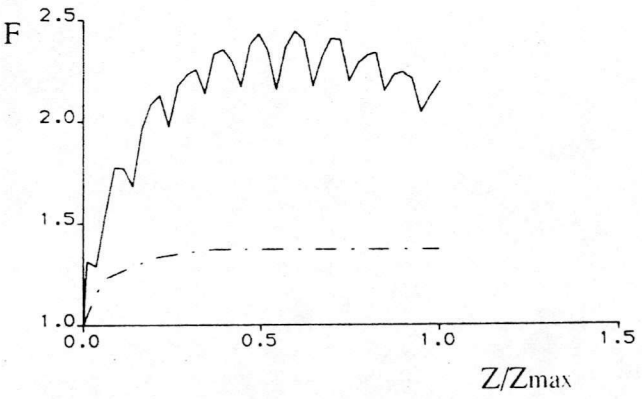

f) r/R = 1.0

Calculated ————————

Prescribed · — —— — ·

Figure 4.2 Comparison between prescribed and calculated axial induced velocities : $\lambda = 8.0$

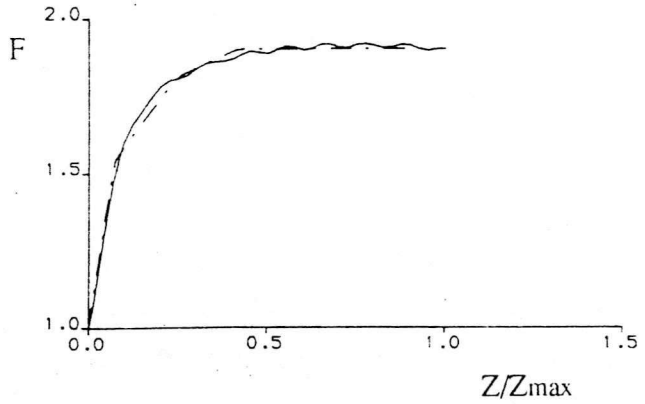

a) r/R = 0.226

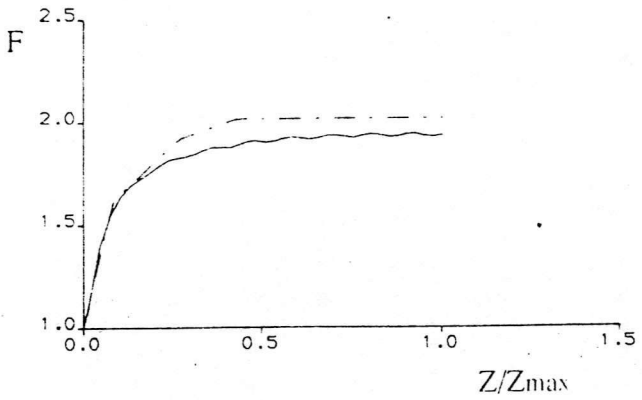

b) r/R = 0.321

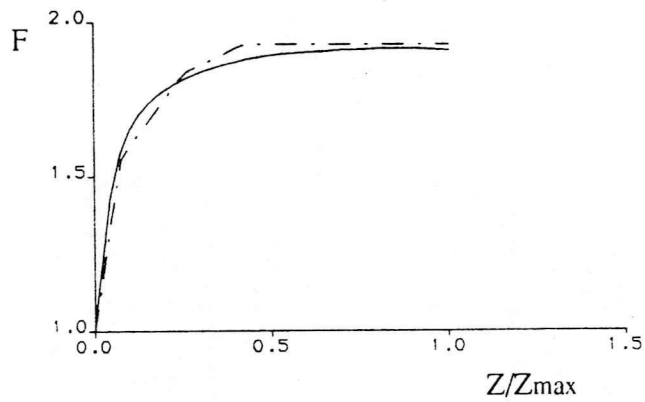

c) r/R = 0.570

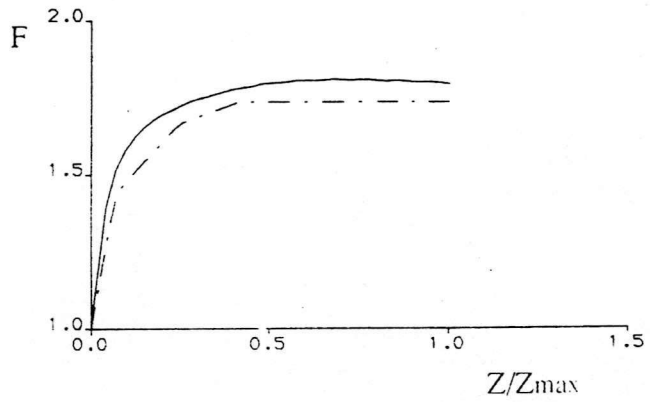

d) r/R = 0.771

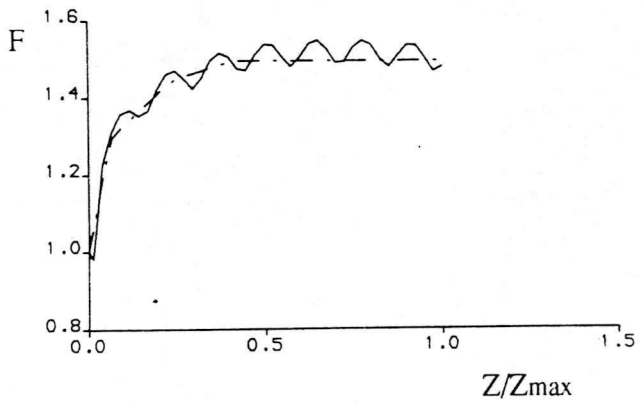

e) r/R = 0.880

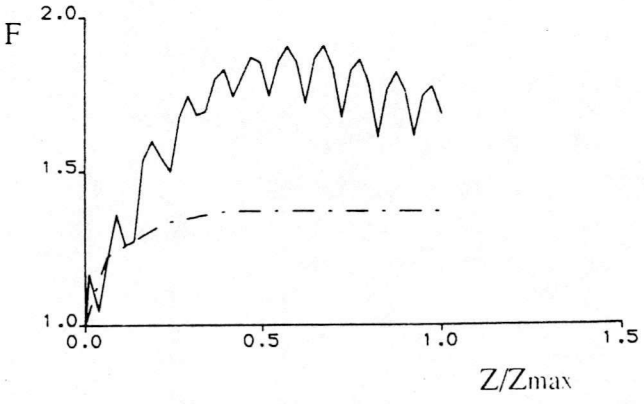

f) r/R = 1.0

Calculated ————————

Prescribed · — —— — ·

Figure 4.3 Comparison between prescribed and calculated axial induced velocities : $\lambda = 9.0$

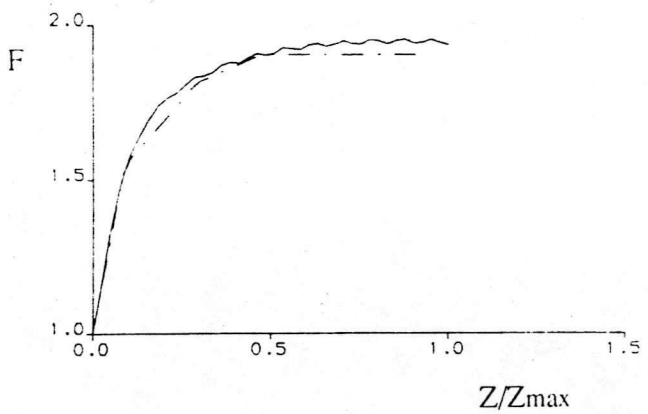

a) r/R = 0.226

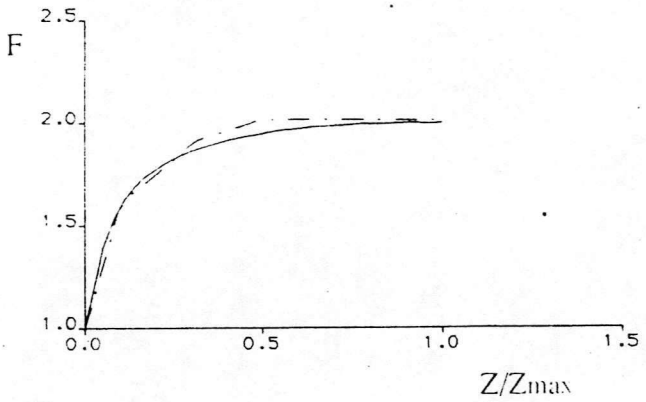

b) r/R = 0.321

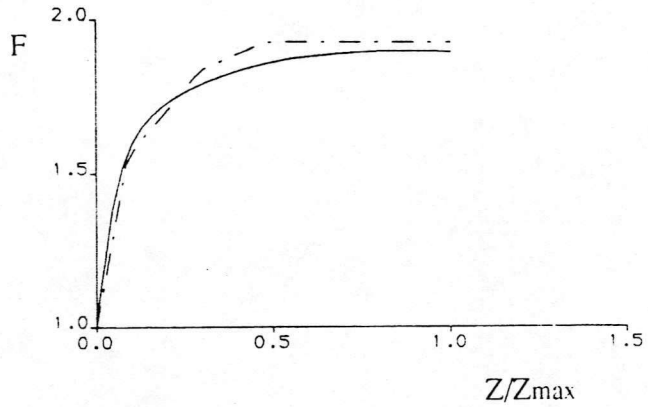

c) r/R = 0.570

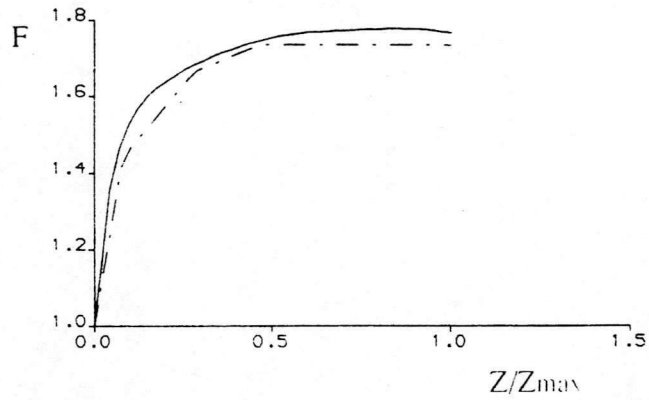

d) r/R = 0.771

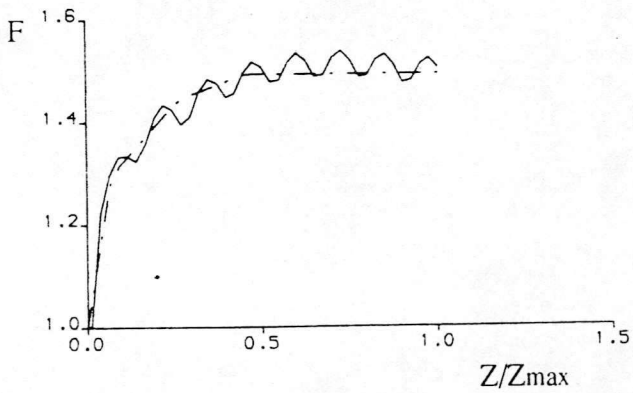

e) r/R = 0.880

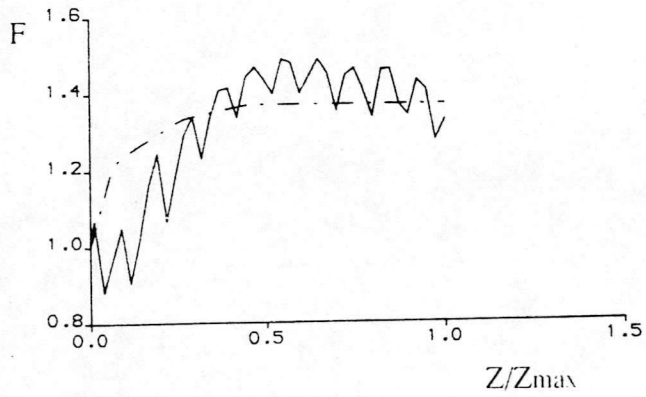

f) r/R = 1.0

Calculated ————————

Prescribed · — —— — ·

Figure 4.4 Comparison between prescribed and calculated axial induced velocities : $\lambda = 10.0$

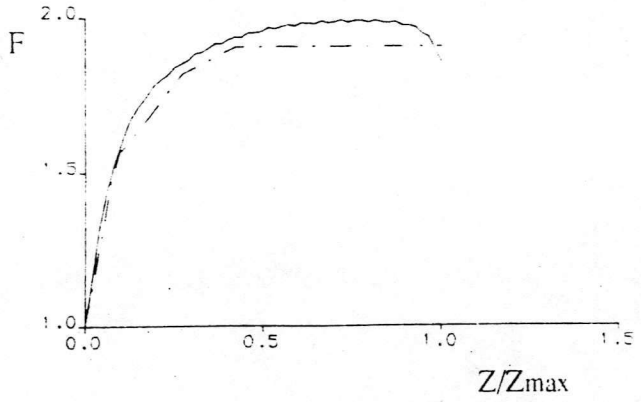

a) r/R = 0.226

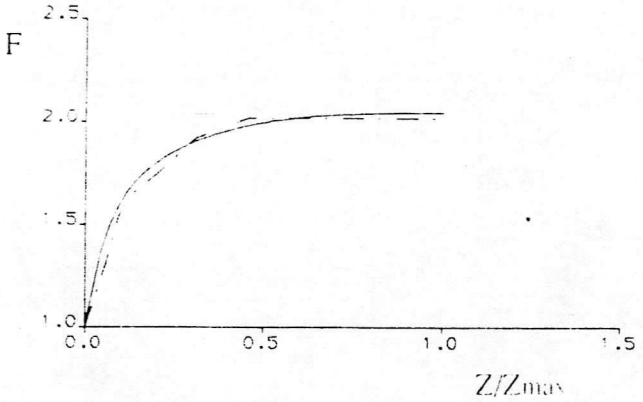

b) r/R = 0.321

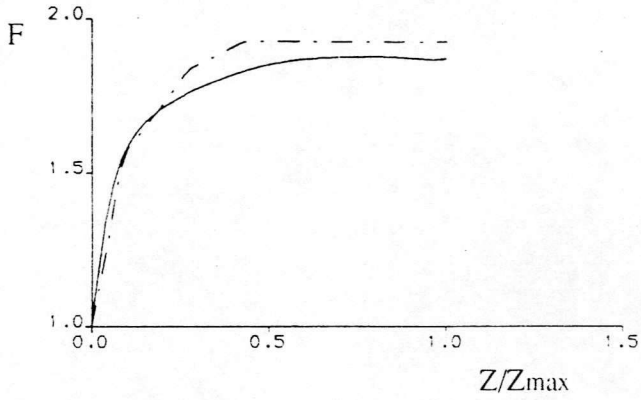

c) r/R = 0.570

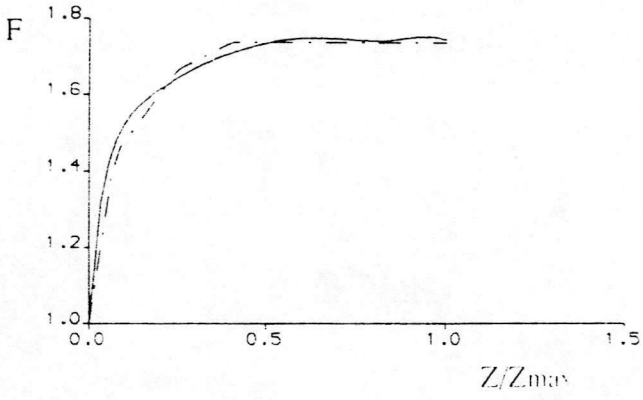

d) r/R = 0.771

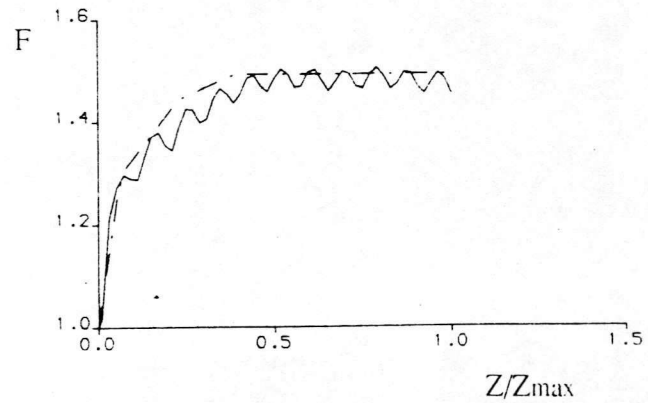

e) r/R = 0.880

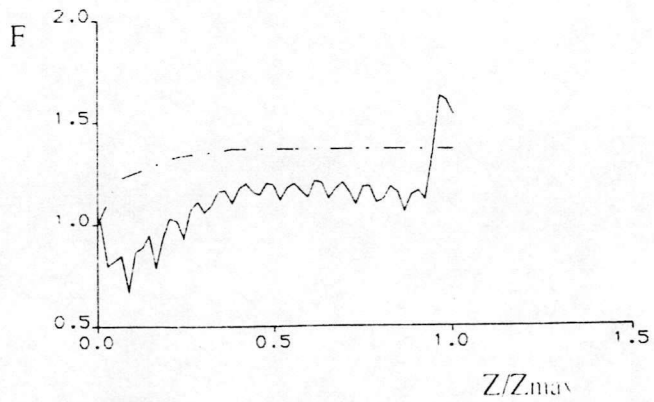

f) r/R = 1.0

Calculated ————————

Prescribed · — —— — ·

Figure 4.5 Comparison between prescribed and calculated axial induced velocities : $\lambda = 11.0$

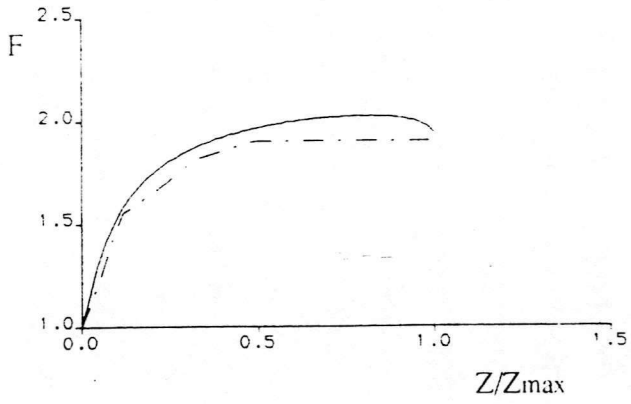

a) r/R = 0.226

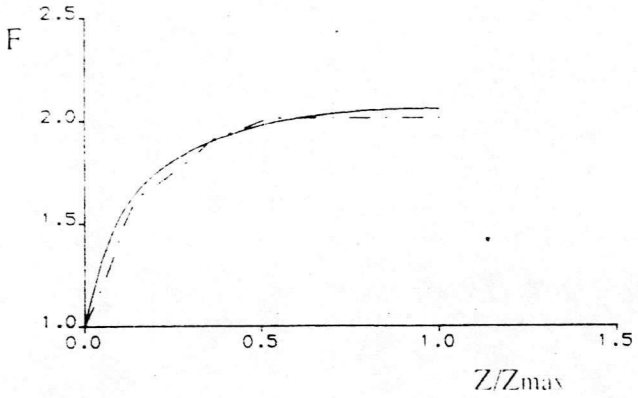

b) r/R = 0.321

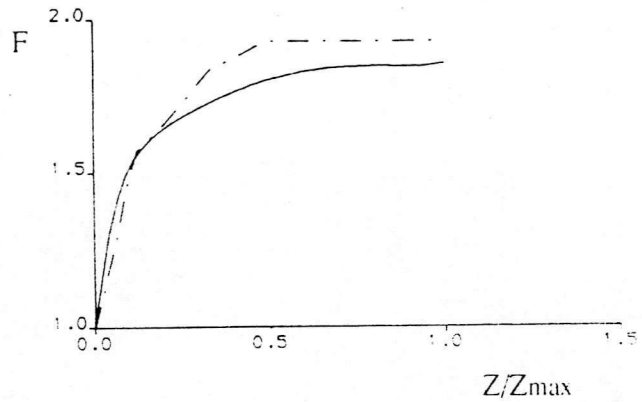

c) r/R = 0.570

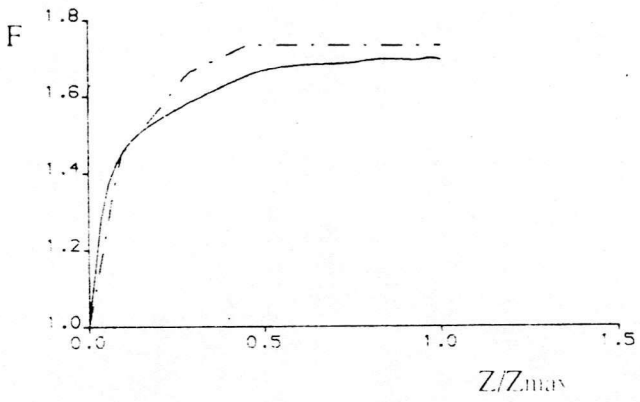

d) r/R = 0.771

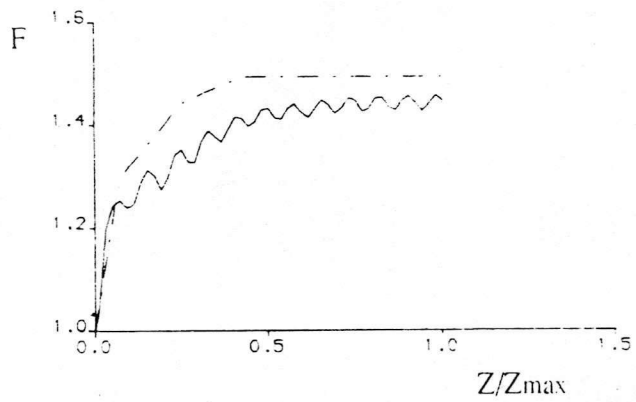

e) r/R = 0.880

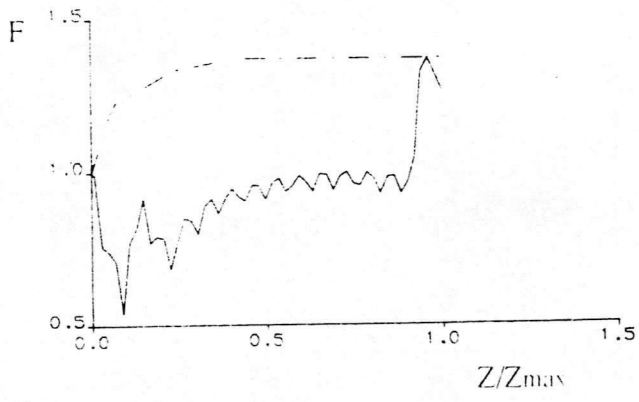

f) r/R = 1.0

Calculated ————————

Prescribed — —— — —

Figure 4.6 Comparison between prescribed and calculated axial induced velocities : $\lambda = 12.0$

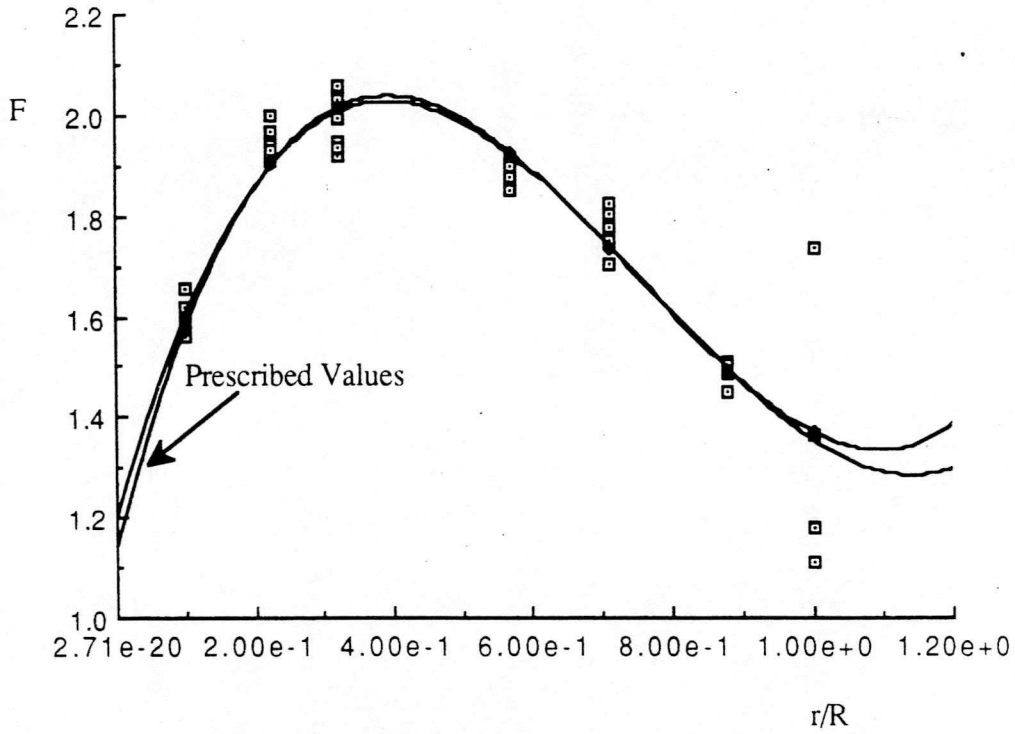

Figure 4.7 Comparison of prescribed and calculated far wake conditions : λ = 7.0 - 12.0

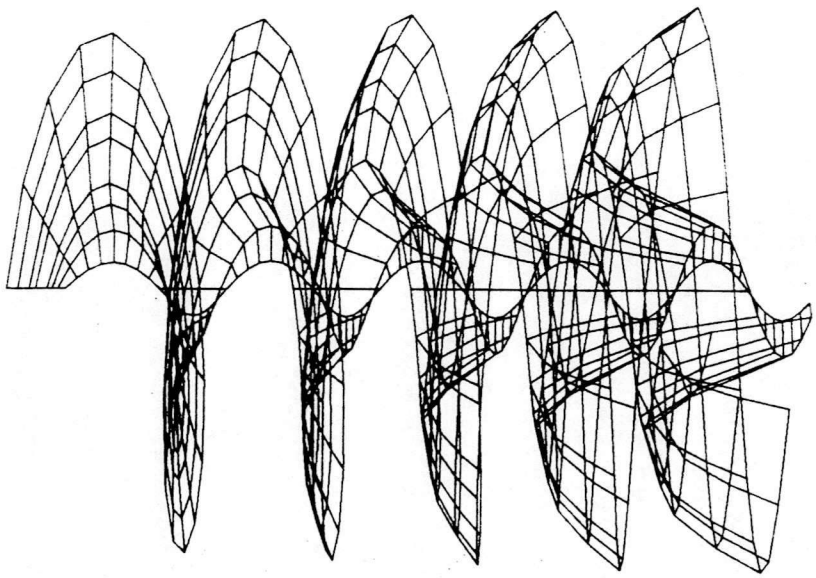

a)First iteration

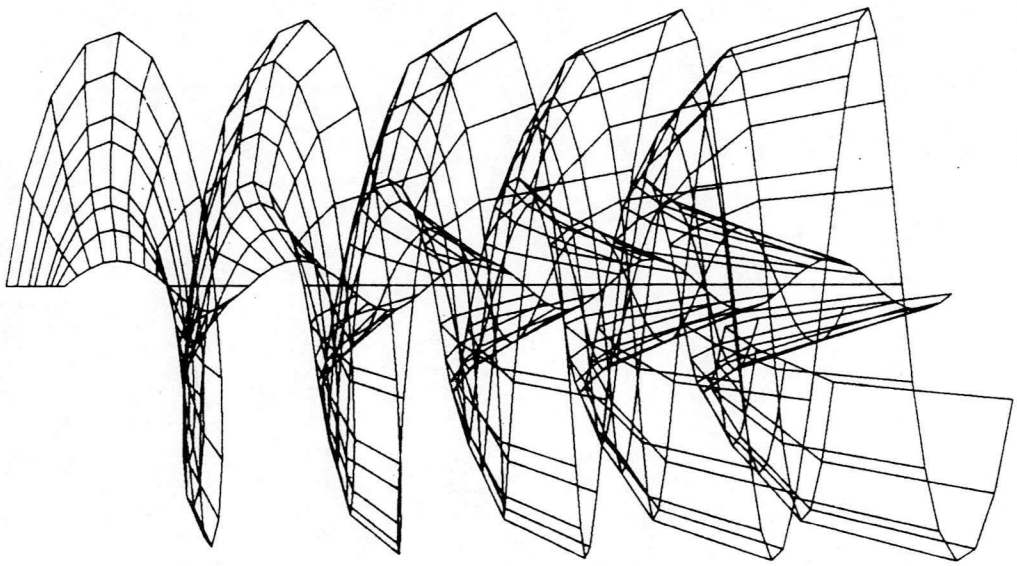

b) Second iteration

Figure 4.8 Wake geometry trailed from single blade at $\lambda = 9.0$

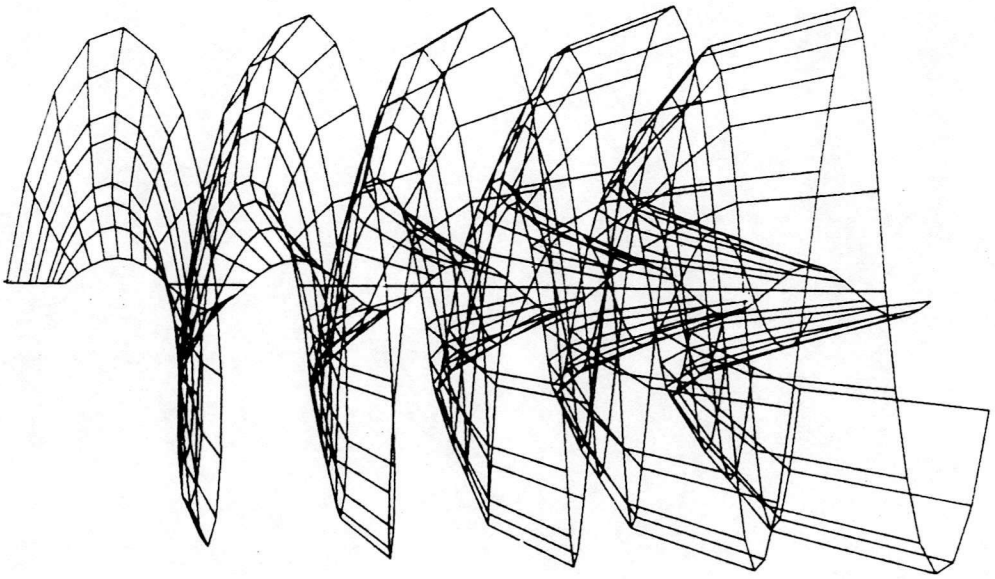

c) Third iteration

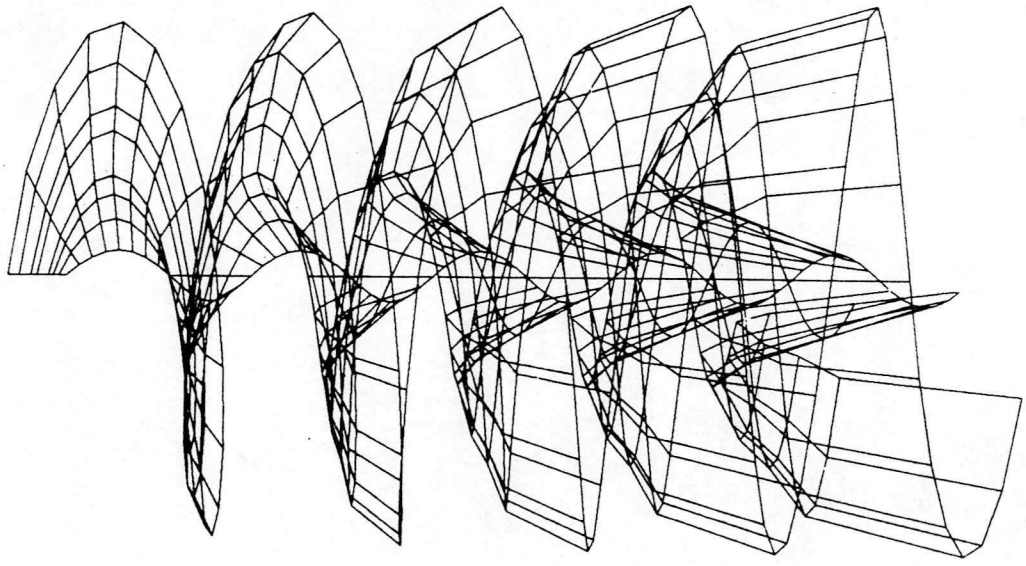

d) Fourth iteration

Figure 4.8 Wake geometry trailed from single blade at $\lambda = 9.0$

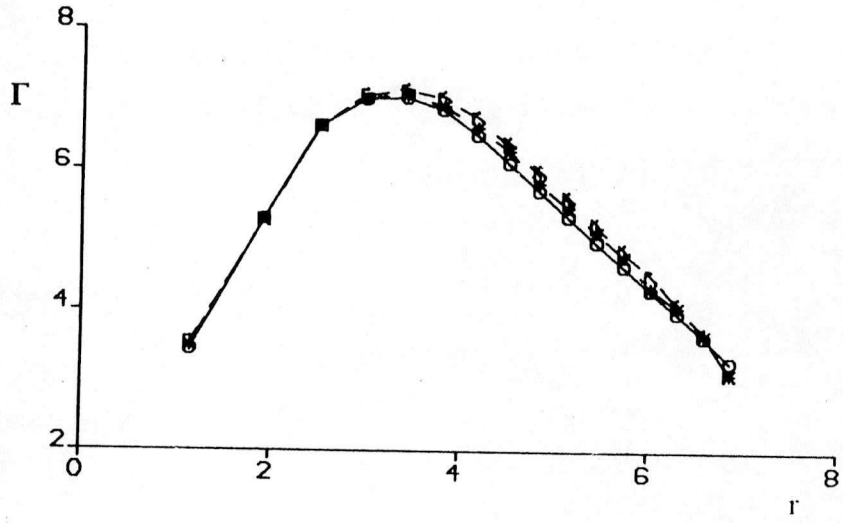

a) Iterations 1 - 4

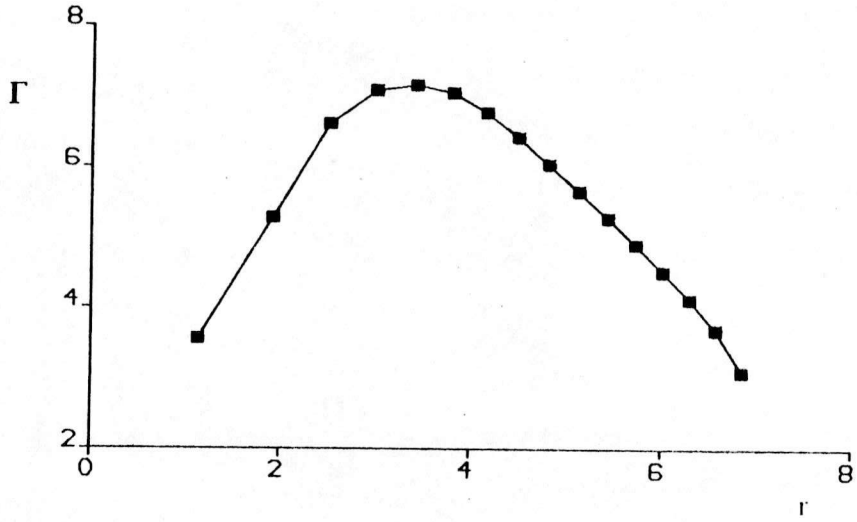

b) Iterations 5 - 8

1 2 3 4

5 6 7 8

Figure 4.9 Evolution of blade loading over eight iterations, $\lambda = 7.0$

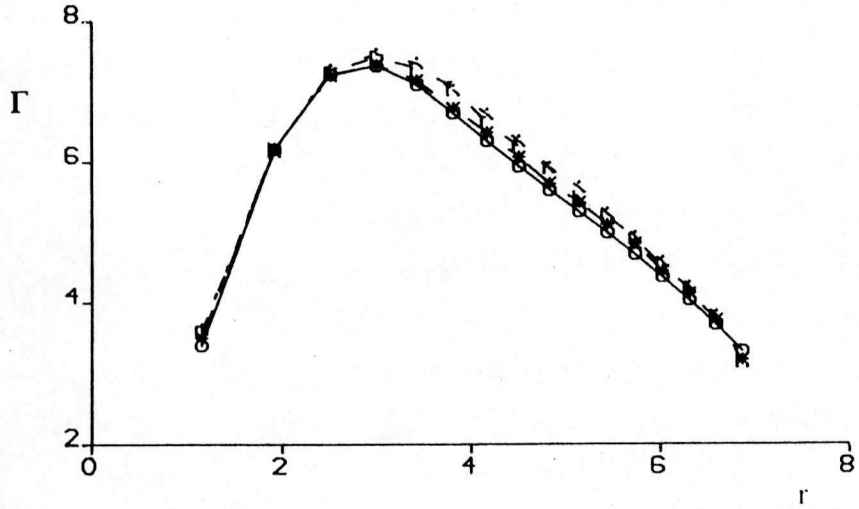

a) Iterations 1 - 4

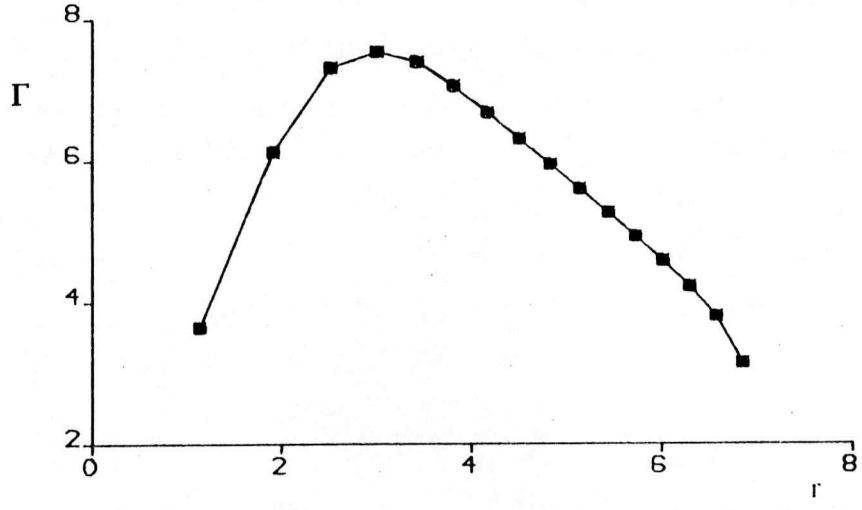

b) Iterations 5 - 8

1 2 3 4 5 6 7 8

Figure 4.10 Evolution of blade loading over eight iterations, $\lambda = 8.0$

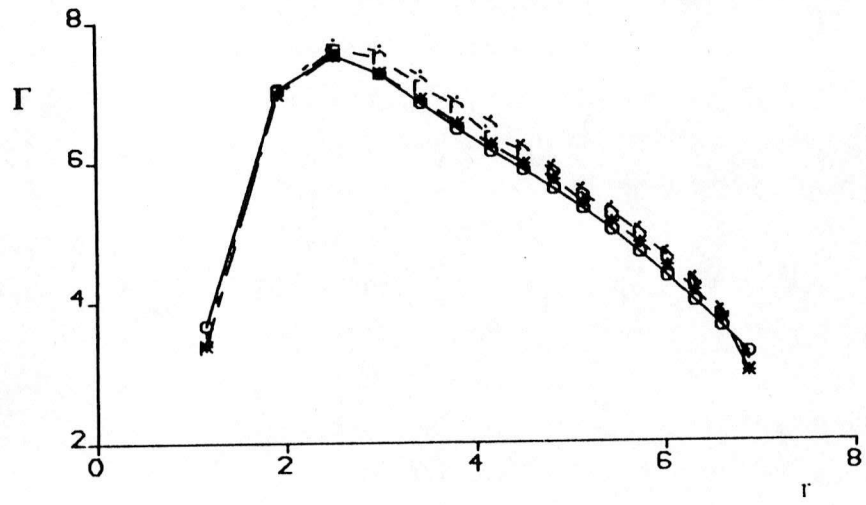

a) Iterations 1 - 4

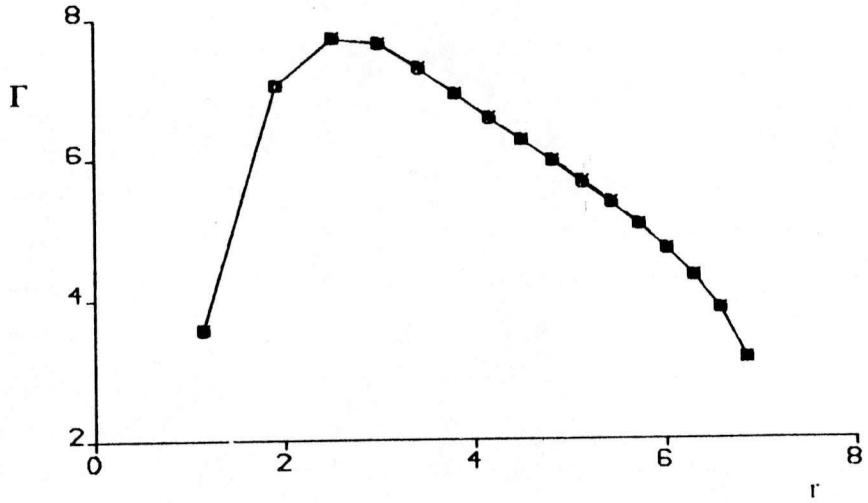

b) Iterations 5 - 8

1 2 3 4 5 6 7 8

Figure 4.11 Evolution of blade loading over eight iterations, $\lambda = 9.0$

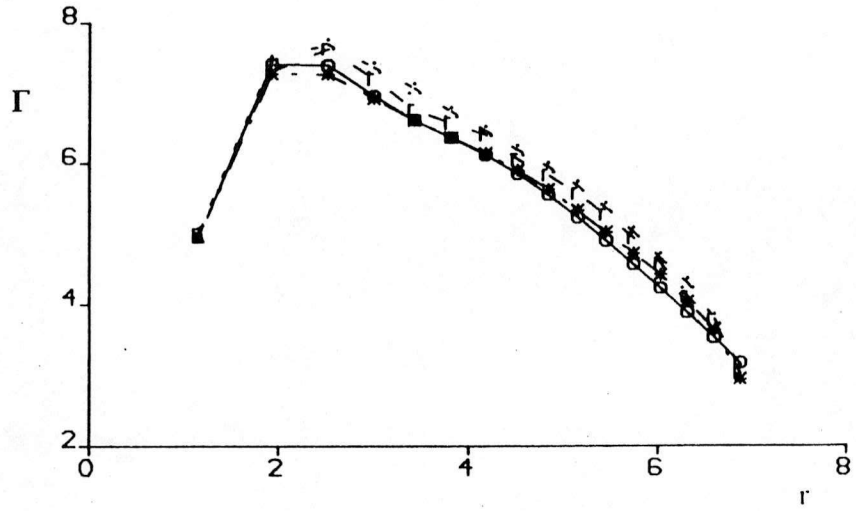

a) Iterations 1 - 4

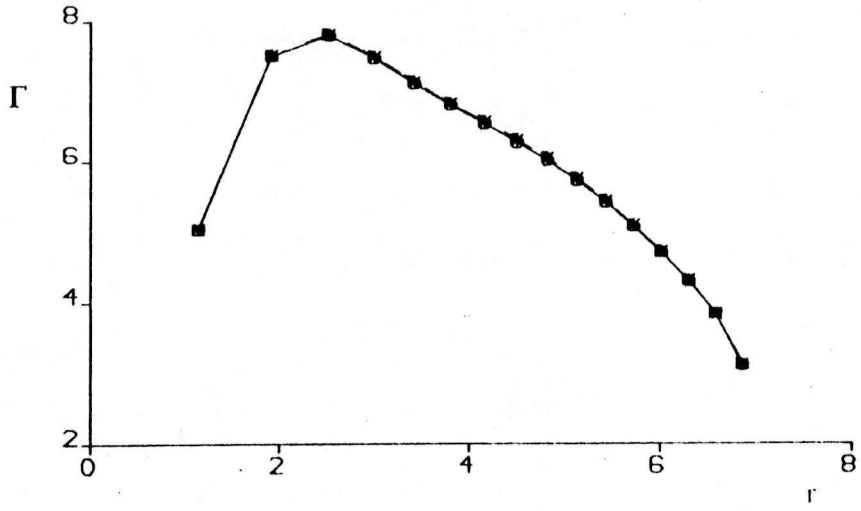

b) Iterations 5 - 8

1 2 3 4

5 7 6 8

Figure 4.12 Evolution of blade loading over eight iterations, $\lambda = 10.0$

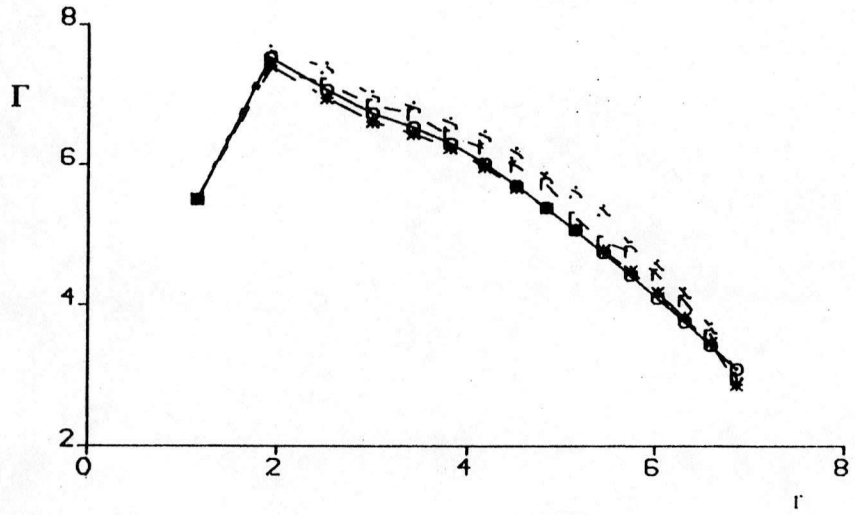

a) Iterations 1 - 4

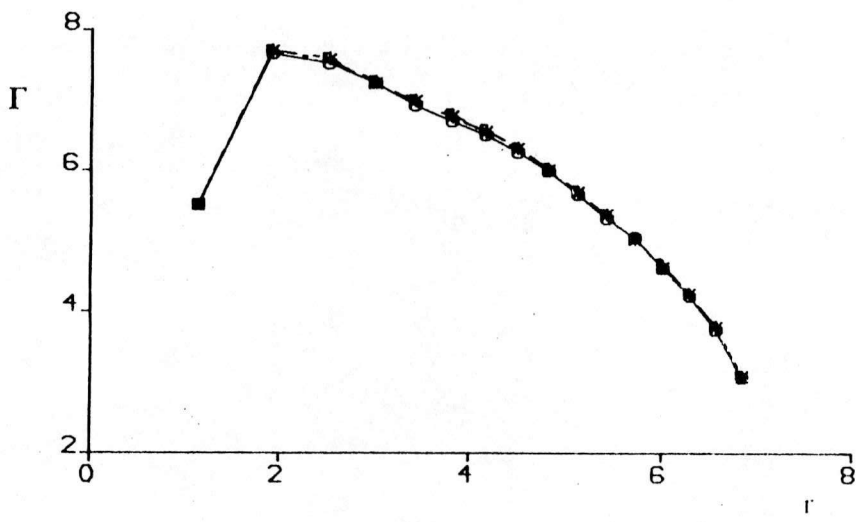

b) Iterations 5 - 8

1 2

3 4

5 7

6 8

Figure 4.13 Evolution of blade loading over eight iterations, $\lambda = 11.0$

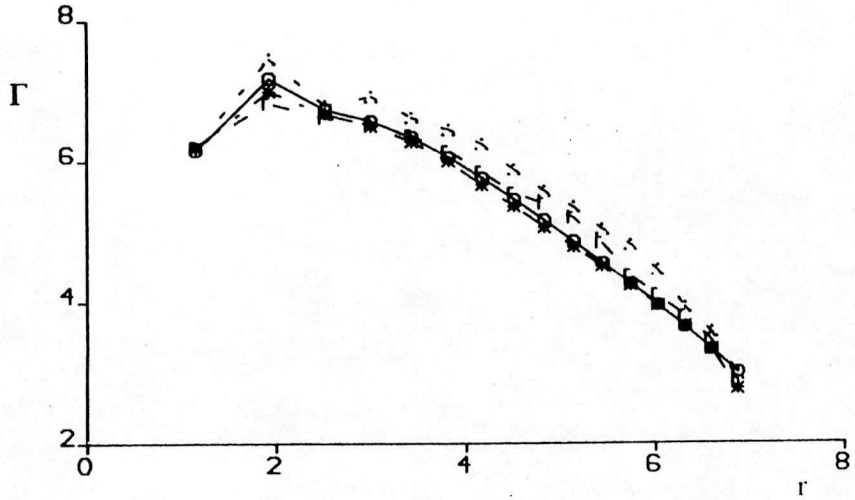

a) Iterations 1 - 4

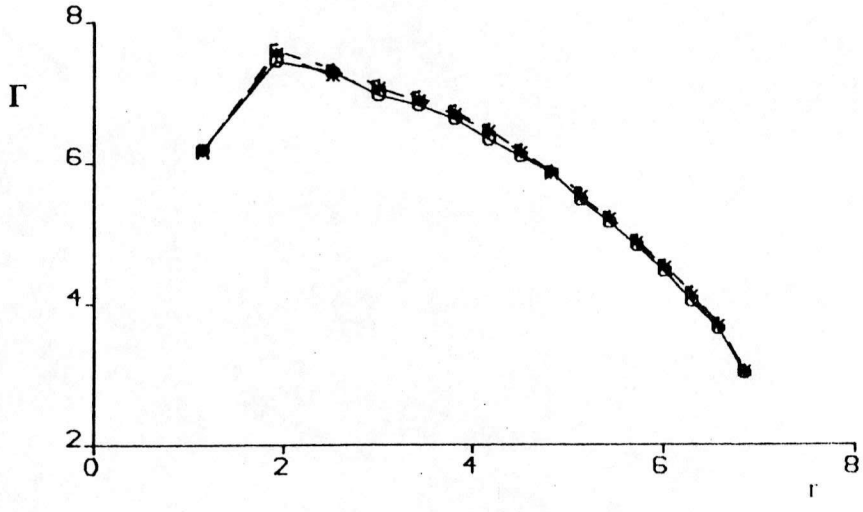

b) Iterations 5 - 8

1 2 3 4

5 6 7 8

Figure 4.14 Evolution of blade loading over eight iterations, $\lambda = 12.0$

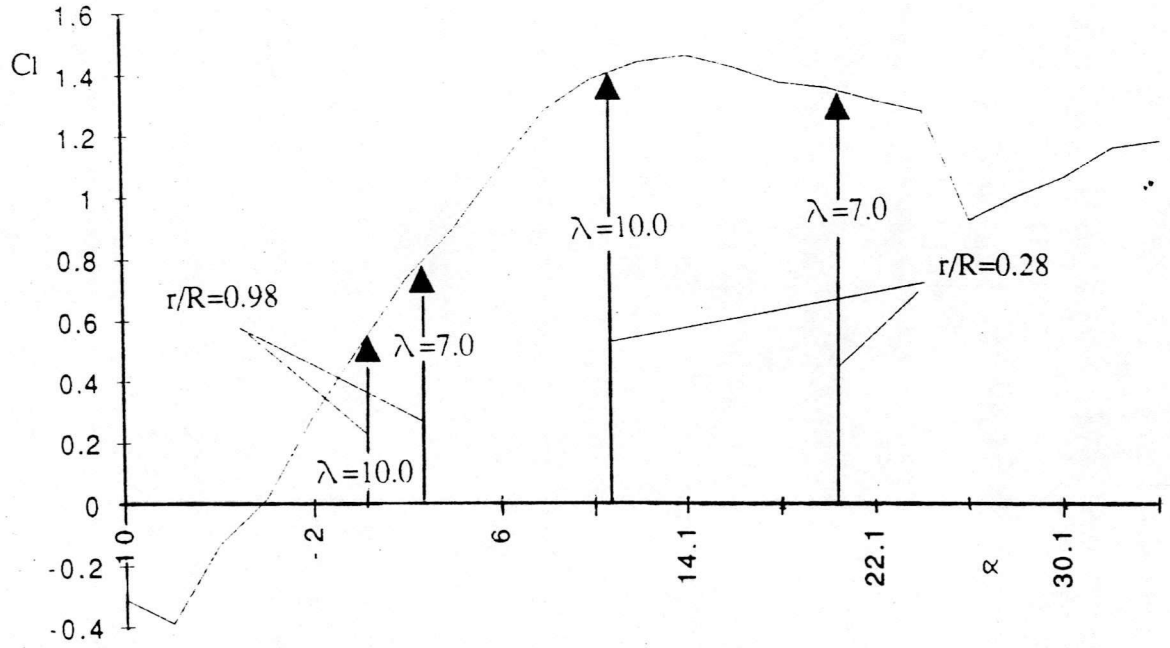

Figure 4.15 Effect of increasing λ on blade incidence and Cl

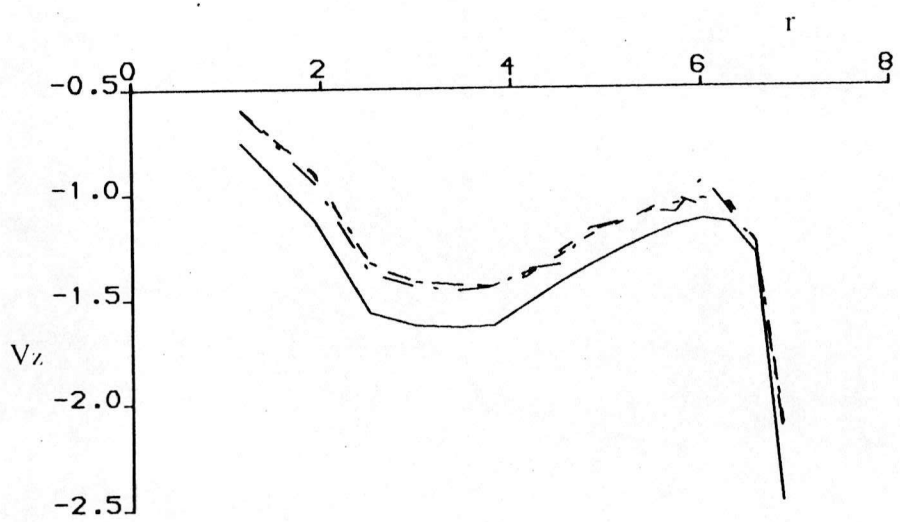

a) Iterations 1 - 4

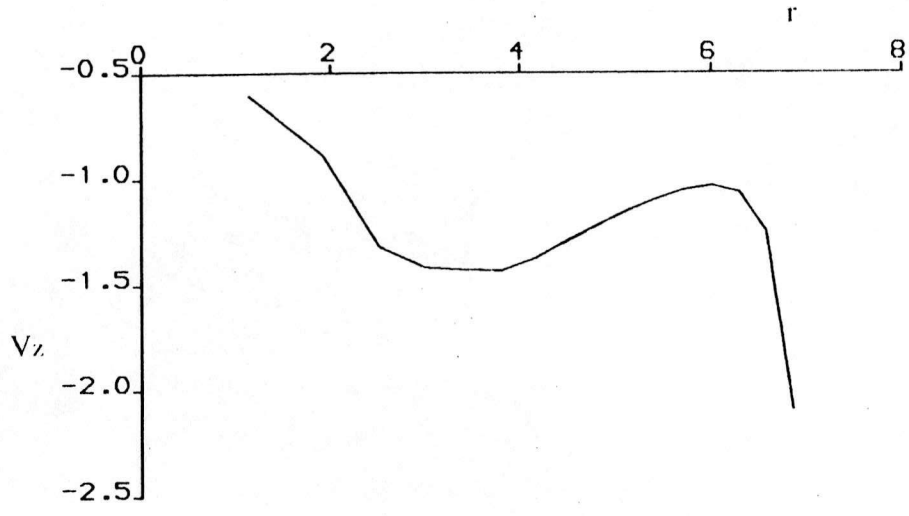

b) Iterations 5 - 8

1 —————— 2 - - —— - -

3 - - - - - - 4 ---------

5 —————— 7 - - —— - -

6 - - - - - - 8 ---------

Figure 4.16 Evolution of spanwise induced velocities over eight iterations, $\lambda = 7.0$

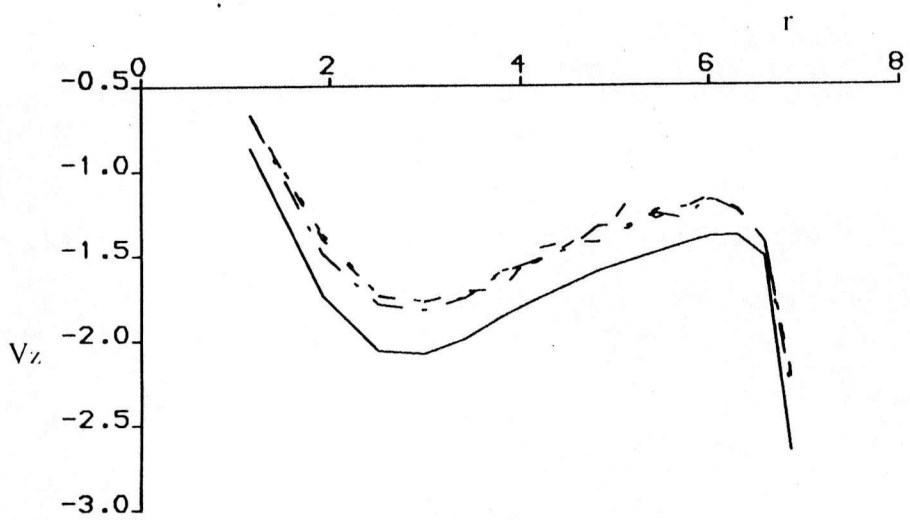

a) Iterations 1 - 4

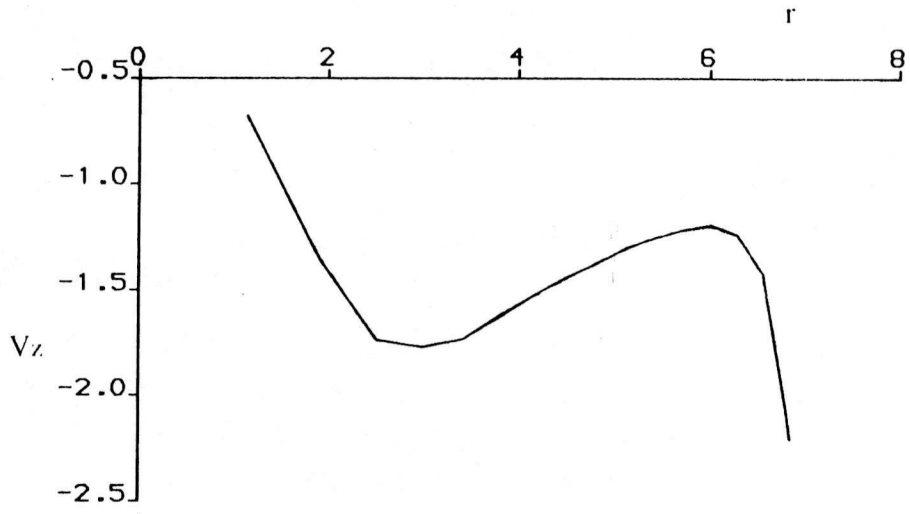

b) Iterations 5 - 8

1 2
3 4

5 7
6 8

Figure 4.17 Evolution of spanwise induced velocities over eight iterations, $\lambda = 8.0$

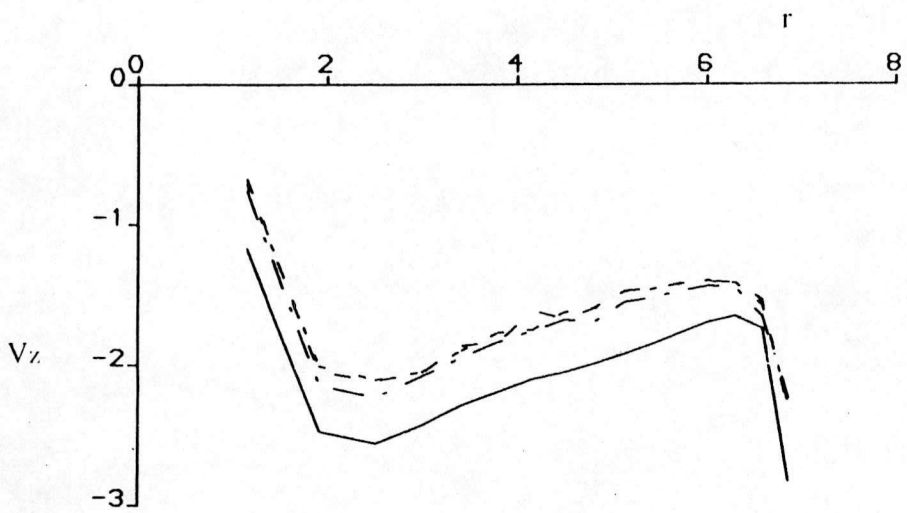

a) Iterations 1 - 4

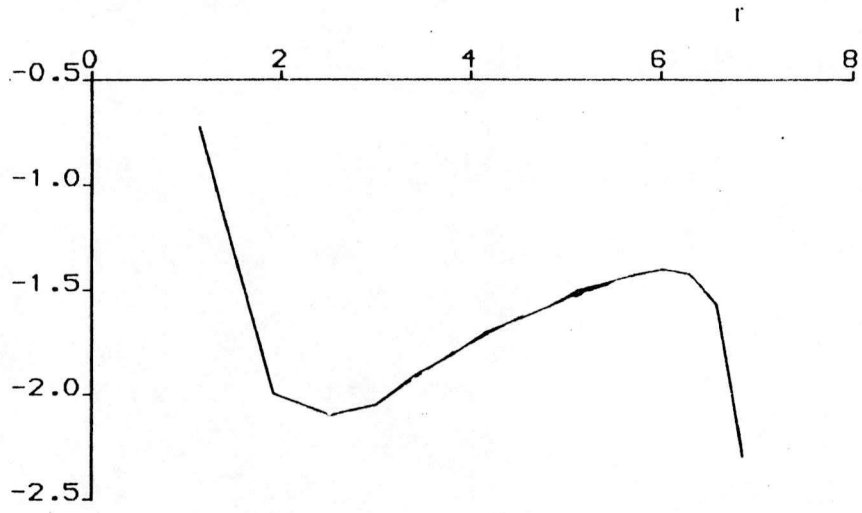

b) Iterations 5 - 8

1 —————— 2 – – —— – –

3 – – – – – 4 ————————

5 —————— 7 – – —— – –

6 – – – – – 8 ————————

Figure 4.18 Evolution of spanwise induced velocities over eight iterations, $\lambda = 9.0$

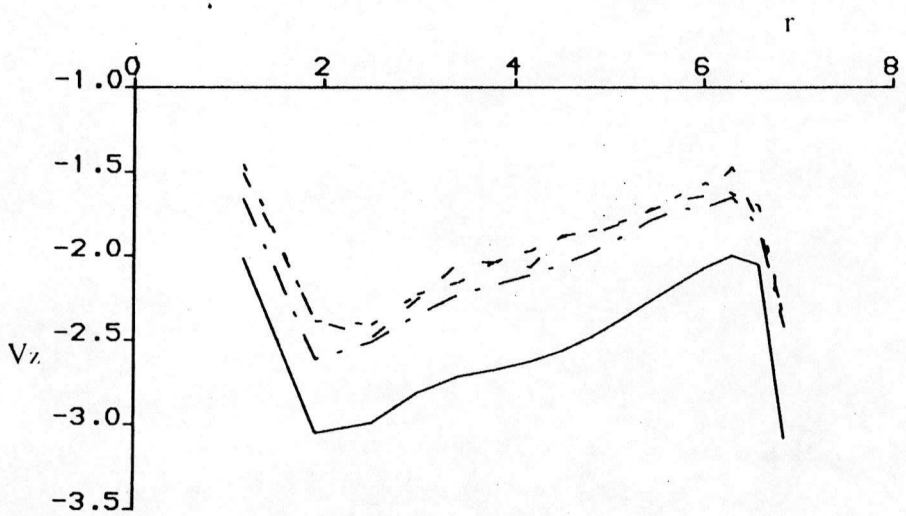

a) Iterations 1 - 4

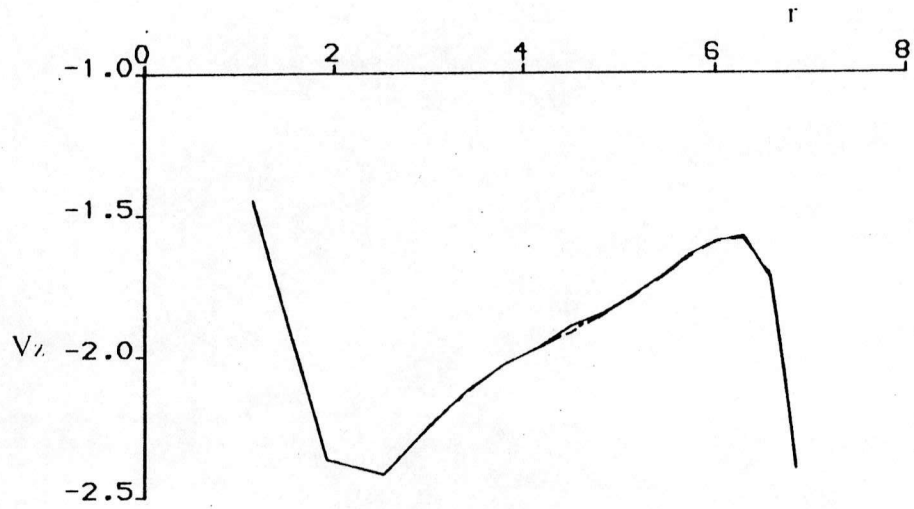

b) Iterations 5 - 8

1 —————— 2 – – —— – –

3 – – – – – 4 ————————

5 —————— 7 – – —— – –

6 – – – – – 8 ————————

Figure 4.19 Evolution of spanwise induced velocities over eight iterations, $\lambda = 10.0$

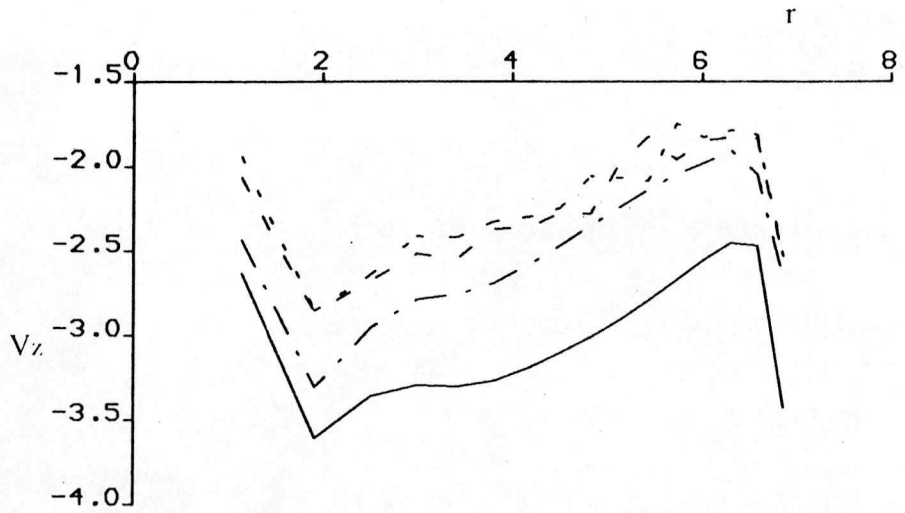

a) Iterations 1 - 4

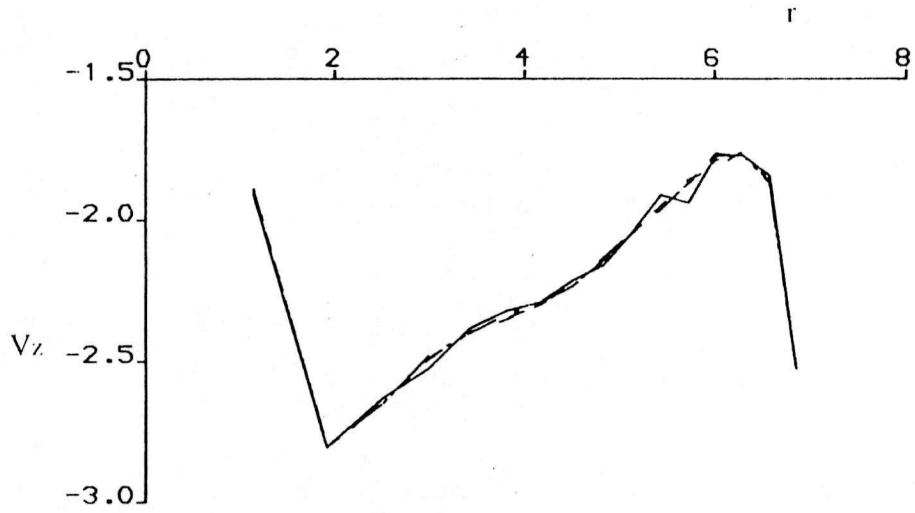

b) Iterations 5 - 8

1 —————— 2 - - —— - -

3 - - - - - - 4 ----------

5 —————— 7 - - —— - -

6 - - - - - - 8 ----------

Figure 4.20 Evolution of spanwise induced velocities over eight iterations, $\lambda = 11.0$

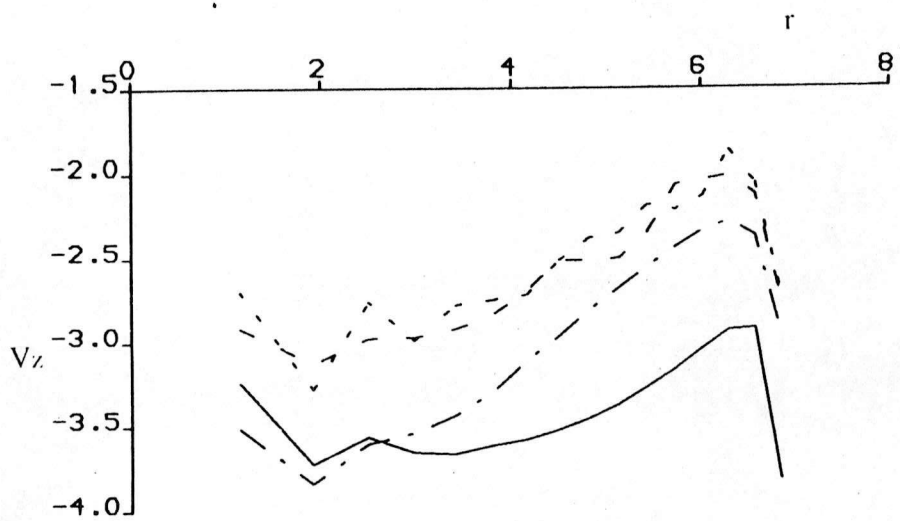

a) Iterations 1 - 4

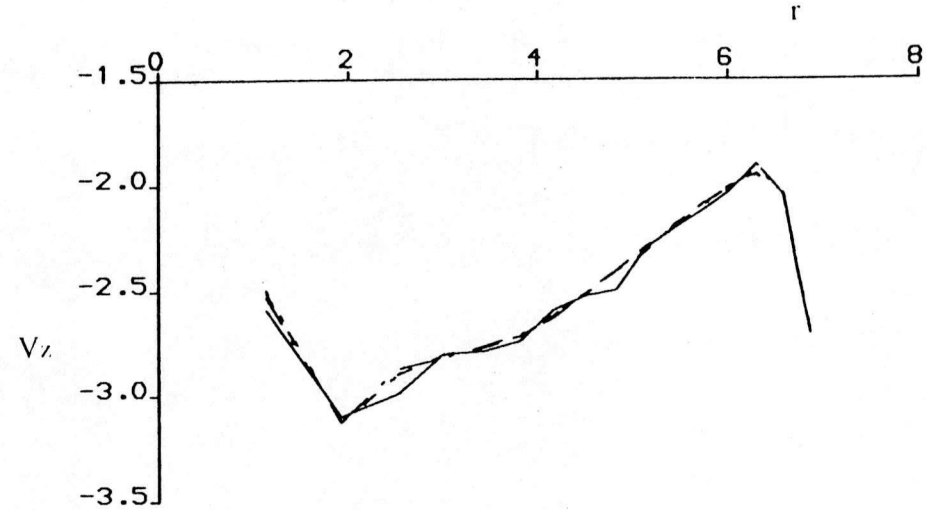

b) Iterations 5 - 8

1 —————— 2 – – —— – –

3 – – – – – 4 ———————

5 —————— 7 – – —— – –

6 – – – – – 8 ———————

Figure 4.21 Evolution of spanwise induced velocities over eight iterations, $\lambda = 12.0$

Appendix A

From Fig 2.6 it can be seen that

$$\underline{r}_A = (X - X_A)\underline{i} + (Y - Y_A)\underline{j} + (Z - Z_A)\underline{k} \quad \text{(A.1a)}$$

$$\underline{r}_B = (X - X_B)\underline{i} + (Y - Y_B)\underline{j} + (Z - Z_B)\underline{k} \quad \text{(A.1b)}$$

$$\underline{r}_{AB} = (X_A - X_B)\underline{i} + (Y_A - Y_B)\underline{j} + (Z_A - Z_B)\underline{k} \quad \text{(A.1c)}$$

From equations (A.1a) and (A.1b) we obtain

$$|\underline{r}_A| = \sqrt{[(X - X_A)^2 + (Y - Y_A)^2 + (Z - Z_A)^2]} \quad \text{(A.2a)}$$

$$|\underline{r}_B| = \sqrt{[(X - X_B)^2 + (Y - Y_B)^2 + (Z - Z_B)^2]} \quad \text{(A.2b)}$$

The cross product term in equation (2.41) expands to

$$\underline{r}_A \times \underline{r}_B = \begin{vmatrix} i & j & k \\ X - X_A & Y - Y_A & Z - Z_A \\ X - X_B & Y - Y_B & Z - Z_B \end{vmatrix}$$

$$\begin{aligned} &= [(Y - Y_A)(Z - Z_B) - (Y - Y_B)(Z - Z_A)]\,\underline{i} \\ &- [(X - X_A)(Z - Z_B) - (X - X_B)(Z - Z_A)]\,\underline{j} \\ &+ [(X - X_A)(Y - Y_B) - (X - X_B)(Y - Y_A)]\,\underline{k} \end{aligned} \quad \text{(A.3)}$$

and therefore

$$\begin{aligned} |\underline{r}_A \times \underline{r}_B|^2 &= [(Y - Y_A)(Z - Z_B) - (Y - Y_B)(Z - Z_A)]^2 \\ &- [(X - X_A)(Z - Z_B) - (X - X_B)(Z - Z_A)]^2 \\ &+ [(X - X_A)(Y - Y_B) - (X - X_B)(Y - Y_A)]^2 \end{aligned} \quad \text{(A.4)}$$

Appendix B

From equation (2.6), for a given blade element bound vorticity Γ_b

$$\frac{\partial \Gamma_b}{\partial v_{Zn}} = \frac{\partial}{\partial v_{Zn}}\left(\tfrac{1}{2} V_R c C_L\right)$$

$$= \frac{\partial V_R}{\partial v_{Zn}}\left(\tfrac{1}{2} c C_L\right) + \frac{\partial C_L}{\partial v_{Zn}}\left(\tfrac{1}{2} V_R c\right) \qquad \text{(B.1)}$$

The resultant velocity V_R is given by

$$V_R = \sqrt{\left(U_\infty - v_{Zn}\right)^2 + \left(\Omega r + v_{Xn}\right)^2 + v_{Yn}{}^2} \qquad \text{(B.2)}$$

The tangential induced velocity, v_{Yn}, was found to be small in comparison with Ωr. In order retain numerical efficiency it was therefore decided to treat this term as a constant within the iterative procedure rather than iterate towards a solution simultaneously with v_{Zn}. For the same reasons, the radial induced velocity v_{Xn} was also treated as a constant within the iterative procedure as it's influence on the blade conditions is small. Both v_{Xn} and v_{Yn} are re-evaluated on completion of the iteration procedure.

Thus,

$$\frac{\partial V_R}{\partial v_{Zn}} = \frac{\partial}{\partial v_{Zn}}\left[\left[\left(U_\infty + v_{Zn}\right)^2 + \left(\Omega r + v_{Yn}\right)^2 + v_{Xn}{}^2\right]^{1/2}\right]$$

$$= \frac{\left(U_\infty + v_{Zn}\right)}{\left[\left(U_\infty + v_{Zn}\right)^2 + \left(\Omega r + v_{Yn}\right)^2 + v_{Xn}{}^2\right]^{1/2}} \qquad \text{(B.3)}$$

Using the chain rule, the term $\frac{\partial C_L}{\partial v_{Zn}}$ in equation (B.1) may be expressed as

$$\frac{\partial C_L}{\partial v_{Zn}} = \frac{\partial \alpha}{\partial v_{Zn}} \frac{\partial C_L}{\partial \alpha} \qquad \text{(B.4)}$$

where $\frac{\partial C_L}{\partial \alpha}$ is the lift curve slope.

The angle of attack, α is given by

$$\alpha = \tan^{-1}\left(\frac{(U_\infty + v_{Zn})}{(\Omega r + v_{Yn})}\right) - \theta \qquad \text{(B.5)}$$

Now, letting $m = \frac{(U_\infty + v_{Zn})}{(\Omega + v_{Yn})r}$, and using the chain rule, the term $\frac{\partial \alpha}{\partial v_{Zn}}$ may be expressed as

$$\frac{\partial \alpha}{\partial v_{Zn}} = \frac{\partial \alpha}{\partial m}\frac{\partial m}{\partial v_{Zn}} \qquad \text{(B.6)}$$

where

$$\frac{\partial \alpha}{\partial m} = \frac{\partial}{\partial m}\left(\tan^{-1} m - \theta\right)$$

$$= \left(1 + m^2\right)^{-1} \qquad \text{(B.7)}$$

and

$$\frac{\partial m}{\partial v_{Zn}} = \frac{\partial}{\partial v_{Zn}}\left[\frac{(U_\infty + v_{Zn})}{(\Omega r + v_{Yn})}\right]$$

$$= \frac{1}{(\Omega r + v_{Yn})} \qquad \text{(B.8)}$$

Expanding equation (B.8) gives

$$\frac{\partial \alpha}{\partial m} = \left[1 + \left(\frac{(U_\infty + v_{Zn})}{(\Omega r + v_{Yn})}\right)^2\right]^{-1}$$

$$= \frac{(\Omega r + v_{Yn})^2}{(U_\infty + v_{Zn})^2 + (\Omega r + v_{Yn})^2} \qquad \text{(B.9)}$$

As stated previously v_X is small in relation to the other velocity terms, thus equation (B.9) may be written

$$\frac{\partial \alpha}{\partial m} \approx \frac{(\Omega r + v_{Yn})^2}{V_R^2}$$

$$= \cos^2 \phi \qquad \text{(B.10)}$$

Substituting equations (B.8) and (B.10) into equation (B.6) gives

$$\frac{\partial \alpha}{\partial v_{Zn}} = \frac{\cos^2 \phi}{(\Omega r + v_{Yn})} \qquad \text{(B.11)}$$

Hence, equation (B.4) becomes

$$\frac{\partial C_L}{\partial v_{Zn}} = \frac{\partial C_L}{\partial \alpha} \frac{\cos^2 \phi}{(\Omega r + v_{Yn})} \qquad \text{(B.12)}$$

Substituting equations (B.3) and (B.12) into equation (B.1) gives

$$\frac{\partial \Gamma_b}{\partial v_{Zn}} = \tfrac{1}{2} c \left[\frac{(U_\infty - v_{Zn})}{V_R} C_L + V_R \frac{\partial C_L}{\partial \alpha} \frac{\cos^{2\phi}}{(\Omega r + v_{Yn})} \right] \qquad \text{(B.13)}$$

References

1. Butterfield, C.P. et al. 'Spanwise aerodynamic loads on a rotating blade', SERI/TP-257-3983, UC Category : 261, DE 91002101, (Wind Power, October 1990)

2. Miller, R.H. 'Aerodynamics of horizontal axis wind turbines', Wind Energy Conversion vol II, Massachusetts Institute of Technology, Cambridge (U.S.A), Sept 1978.

3. Wilson, R.E. et al. 'Aerodynamic performance of wind turbines', Oregon State University, Corvallis U.S.A, Dept. of Mechanical Engineering, June 1976.

4. Anderson, M.B. 'A vortex wake analysis of a horizontal axis wind turbine and a comparison with a modified blade element theory', Third International Symposium on Wind Energy Systems, August 1980.

5. Rosen, A., Lavie, I. and Seginer, A. 'A general free wake efficient analysis of horizontal axis wind turbines', Wind Engineering, vol 14, No 6 1990.

6. Zevros, A., Huberson, S. and Hemon, A. 'Three-dimensioinal free wake calculation of wind turbine wakes', Journal of Wind Engineering and Industrial Aerodynamics, 27 (1988) 65 - 76.

7. Basuno, B. 'A prescribed wake model for vertical axis wind turbines', Ph.D thesis, Department of Aerospace Engineering, University of Glasgow, 1992.

8. Landgrebe, A.J. 'An analytical method for predicting rotor wake geometry', AIAA, AHA VTOL research, design and operations meeting, Atlanta, Georgia, Feb 1969.

9. Robison, D.J. 'The validation of a scattered light measurement technique for the estimation of airborne particle residence time in the wakes of bluff bodies', T.U München, FLM-Nr-92/13, June 1992.

10. Ostowari, C. and Naik, D. ' Post stall studies of untwisted, varying aspect ratio blades with a NACA 4415 airfoil section - part 1', Wind Engineering, vol 8, No 3 p 176, 1984.

11. Bareiß, R. and Wagner, S. 'Load calculations on rotor blades of a wind turbine', Fifth IEA Symposium, December 1991.

12. Dept. of Energy, 'Design and analysis techniques for wind turbines in unsteady flow environments', Etsu WN 5004, April 1992.

13. Alfredsson, P.H., Dahlberg, J.A. and Bark, F.H. 'Some properties of the wake behind horizontal axis wind turbines', Third International Symposium on Wind Energy Systems, August 1980.

14. Yamane, T., Tsutsui, Y. and Orita, T. 'The aerodynamic performance of a horizontal axis wind turbine in large induced velocity states', Fourth International Symposium on Wind Energy Systems, September 1982.

15. Anderson, M.B., Milborrow, D.J. and Ross, J.N. 'Performance and wake measurements on a 3m diameter horizontal axis wind turbine. Comparison of t theory, wind tunnel and field test data', Fourth International Symposium on Wind Energy Systems, September 1982.

16. Brocklehurst, A. 'Aerodynamic control of horizontal axis wind turbines', Etsu/DEn contract report, Westland Helicopters.

17. Coton, F.N., Galbraith, R.A.McD. and Basuno, B. 'An aerodynamic prediction method for use in vertical axis wind turbine design',